One-Stone-Two-Birds: Over 26% Efficiency in Perovskite Solar Cells via Synergistic Crystallization & Interface Regulation

Boxin Jiao[1,2]†, Liguo Tan[1]†, Yiran Ye[1]†, Ningyu Ren[1]†, Minghao Li[1], Hang Li[1], Xiaoyi Li[2], Chenyi Yi[1,3]*

1 State Key Laboratory of Power System, Department of Electrical Engineering, Tsinghua University, Beijing 100084, China.

2 Center of Materials Science and Optoelectronics Engineering, College of Materials Science and Opto-Electronic Technology, University of Chinese Academy of Sciences, Beijing 100049, China.

3 Institute of Carbon Neutrality, Tsinghua University, Beijing 100084, China.

† These authors contributed equally.

*Corresponding Authors Email: yicy@tsinghua.edu.cn (C. Yi).

Materials and Methods

Materials

Unless otherwise stated, solvents and chemicals were obtained commercially and used without further purification. FTO glass was purchased from Liaoning Preferred New Energy Technology. N,N-dimethylformamide, dimethyl sulfoxide, chlorobenzene (CB, 99.8%, Sigma-Aldrich Inc.), isopropanol, Li-TFSI, PbI_2, gold particles, and PA were obtained from Sigma-Aldrich Inc. 4-tert-butylpyridine was obtained from Aikonchem. FAI, MACl, aqueous solution of PEDOT:PSS, [6,6]-phenyl-C_{61}-butyric acid methyl ester, and spiro-OMeTAD were obtained from Xi'an Polymer Light Technology Corp. $SnCl_2$, urea, thioglycolic acid and hydrochloric acid were obtained from Energy Chemical.

Methods

DFT Calculations

Density functional theory (DFT) calculations are performed by the Vienna Ab Initio Simulation Package with the projector-augmented wave method[1, 2]. The generalized gradient approximation is realized by the Perdew−Burke−Ernzerhof function with projected augmented wave method and the plane-wave energy cutoff of 400 eV[3]. The Monkhorst-Pack k-point grid is set as 4×4×4 for bulk structure optimization (primitive cell structure), and 1×1×1 for heterostructure (perovskite with PA). The DFT+D3 method is adopted for considering van der Waals (vdW) interaction[4]. The convergence criterion for Hellmann-Feynman forces and total energy are set as 0.01 eV/Å and 10^{-5} eV, and a vacuum slab larger than 15 Å is used to avoid the interaction between adjacent images. For density of states calculation, the plane wave cut-off energy of 400 eV is adopted, the energy convergence accuracy is set to 10^{-6} eV, and the force acting on each atom is not greater than 0.01 eV/Å. The Brillouin zone is integrated using a 2×4×1 k-point grid. The interaction energy was calculated by the following equation: E_{int} = *E(Perovskite & PA molecule)-*

E(Perovskite)-E(PA molecule). The formation energy of vacancy defects can be calculated by the following method[5]: $E_{Formation}=E_{defect}+E_{vacancy\ atoms}-E_{total}$. Among them, E_{defect} represents the total energy of the remaining structure after removing vacancy atoms (after structural optimization), $E_{vacancy\ atoms}$ represents the energy of vacancy atoms, and E_{total} represents the total energy of the structure without vacancy defects (after structural optimization).

Quantum chemical calculations are performed using Gaussian09[6]. For the initial structure, using the B3LYP density functional with the 6-311G(d, p) basis set for C, H, N and O elements. Optimized geometries were verified by frequency calculations at the same level of theory as that used for geometry optimization.

Device Fabrication

Perovskite solar cells were fabricated with the following structure: FTO glass (glass/FTO)/SnO_2/Perovskite ($FA_xMA_{1-x}PbI_3$)/Spiro-OMeTAD/Au. The SnO_2 layer is deposited via chemical bath deposition according to literature. After CBD treatment, the glass/FTO/SnO_2 substrate is annealed at 180°C for 1 hour. A 10mmol/L KCl aqueous solution is spin-coated onto the SnO_2 film at a speed of 4000 rpm and annealed at 100°C. Then, the glass/FTO/SnO_2 substrates are transferred into a nitrogen-filled glove box. The PbI_2 solution is prepared by dissolving 1.5 M PbI_2 and 1.2 mg of PA into 1 mL of a mixed DMF/DMSO solvent (v/v 9/1) and heated to 70°C for 2 hours. The amine salt solution is prepared by dissolving 86.5 mg of FAI and 12.5 mg of MACl into 1 mL of IPA. The PbI_2 solution is then spin-coated onto the substrate at 1500 rpm for 30 seconds and annealed at 75°C for 1 minute. The amine salt solution is subsequently spin-coated onto the PbI_2 film at 2000 rpm for 20 seconds, followed by annealing at 40°C for 1 minute in a glove box. After the first annealing step, the film undergoes a second annealing process at 150°C for 15 minutes in an external air environment with 10%-20% humidity. Surface treatment involves spin-coating a PA solution with a concentration of 30 mM (solvent IPA) onto the perovskite thin film at a rotational speed of 4000 rpm. The hole transport layer solution is composed of 72.3 mg of spiro-OMeTAD and 1 mL of chlorobenzene with additives, including 17.5 μL of a Li-TFSI salt solution in acetonitrile (520 mg/mL) and 28.5 μL of 4-tert-butylpyridine. The solution is deposited onto the film by spin-coating at 5000 rpm for 20 seconds. Finally, the devices are fabricated using the vacuum evaporation deposition method to deposit 100 nm of gold.

Characterizations

Unless otherwise specified due to special cases, the PA doping concentration in all PVK-PA films and PSC-PA devices is uniformly 1.2 mg/ml in the perovskite precursor PbI_2 solution.

X-ray diffraction (XRD) was measured by a Rigaku Smart Lab diffractometer with Cu Kα radiation (1.5406 Å). The scan rate was 4°/min at a step-scan size of 0.02°. The perovskite samples for XRD were prepared on glass substrates.

The **in-situ grazing-incidence wide-angle X-ray scattering (GIWAXS)** measurements were completed at beamline 1W1A of the Beijing Synchrotron Radiation Facility. The diffuse scattering experimental station utilizes a dual-focused monochromatic X-ray provided by the 1W1A beamline, and the station adopts a Huber five-circle diffractometer equipped with an EIGER X1M two-dimensional detector for detection. After spin-coating the organic ammonium halide solution, the films were immediately probed before annealing at 25°C. Then, the hot plate was heated up to 150°C at a rate of 100°C/min, and the GIWAXS data was collected every second synchronously.

Scanning electron microscope (SEM) and cross-sectional images of the samples were obtained using a Hitachi S-4700 SEM. The perovskite samples for SEM were prepared on FTO/SnO_2 substrates. The PbI_2 and Perovskite films were fixed onto the sample stage of the SEM using conductive tape. The cross-sectional samples were prepared by scribing the conductive glass backside with a diamond knife and gently breaking it apart. EDS was conducted on the Hitachi S-4700 SEM with INCA PentaFETx3 from Oxford Instruments at 15 kV.

Fourier transform infrared (FTIR) spectra were collected using a Nicolet IS50 spectrometer (Fisher Scientific) in transmittance mode in the range of 400–4,000 cm^{-1}. The samples for FTIR analysis were pure PA powder, PbI_2 films containing PA, and perovskite films containing PA.

Absorption spectra were measured using an **Ultraviolet-visible spectroscopy (UV-vis**) spectrometer (Lambda 45, PerkinElmer) with a scan rate of 4 nm/s. The perovskite layers were prepared on glass, and the monochromatic light was incident on the perovskite side.

Photoluminescence (PL) mappings and **PL lifetime** mappings were collected using Olympus FV1200 Confocal/FLIM/FCS. **Steady-state PL** measurements were conducted on the glass/perovskite samples using a fluorescence spectrometer (Quantaurus Tau C11367-12, Hamamatsu). Time-resolved PL (**TRPL)** was obtained by the PL system combined with a time-correlated single-photon counting (TCSPC) system. The TRPL intensity decay spectra (Fig.S25b) were fitted with the bi-exponential decay function as equation 1, where I_0 is the decay constant, A_1 and A_2 are decay amplitudes, τ_1 is the fast decay time reflecting the interface charge extraction and τ_2 is the slow decay time reflecting the trap-assisted nonradiative charge recombination, as shown in Table S3. The mean fluorescence lifetime τ_{avg} were calculated from the equation 2[7].

$$I(t) = I_0 + A_1 exp(-t/\tau_1) + A_2 exp(-t/\tau_2) \quad (1)$$

$$\tau_{avg} = (A_1\tau_1^2 + A_2\tau_2^2)/(A_1\tau_1 + A_2\tau_2) \quad (2)$$

X-ray photoelectron spectroscopy (XPS) characterization was performed on a Kratos Axis Ultra DLD X-ray Photoelectron Spectrometer by using a monochromatized Al Kα source *(hν*=1486.6 eV).

Time-of-Flight Secondary Ion Mass Spectrometry (ToF-SIMS) was performed with ION ToF-SIMS 5-100 system, the voltage used for sputtering is 1 V.

Kelvin probe force microscopy (**KPFM**) and **conductive atomic force microscopy** (**c-AFM**) measurements were performed using an AFM ICON system (Dimension, Bruker) with a Pt-coated conductive tip under air atmosphere. The KPFM mode, combined with the tapping mode AFM, was used to measure the surface potential signals with an area of 5×5 μm. The c-AFM was conducted using a Pt-coated conductive probe in conductive AFM mode at a 0.5 V direct current (DC) bias voltage. The **AFM** images for morphology scanning were obtained simultaneously during KPFM testing.

The trap density tests measured by **Space charge limited current method (SCLC)** were calculated using equation 3[8]:

$$N_{defect} = \frac{2V_{\mathrm{TFL}}\varepsilon_0\varepsilon_{\mathrm{r}}}{qL^2} \tag{3}$$

Where the voltage of the trap-filled limit (V_{TFL}) is defined as the voltage value at the intersection point of the two fitting lines representing the Ohmic contact and trap-filled regime. ε_{r} and ε_0 are the relative permittivity of the perovskite and the vacuum, respectively, L is the thickness of the films, and q is the electron charge. V_{TFL} is the trap-filled limited voltage. The SCLC tests were measured on devices with the configuration of glass/FTO/SnO_2/perovskite/$PC_{61}BM$/Ag (electron-only devices) and glass/FTO/PEDOT:PSS/perovskite/Spiro-OMeTAD/Ag (hole-only devices), with a voltage range from 0 to 1 V in the dark. In the preparation of electron-only devices, 20mg of $PC_{61}BM$ was dissolved in 1ml of chlorobenzene and then spin-coated onto the perovskite layer for 30 seconds at 2000 rpm in a N_2 glove box. The remaining steps were identical to those in the preparation method for perovskite solar cells (PSCs). For the preparation of hole-only devices, PEDOT:PSS solution was applied to FTO glass by spin-coating for 30 s at 4000 rpm in air, followed by annealing at 150°C for 15 minutes. The remaining steps were also consistent with the preparation method for perovskite solar cells.

The **Mott Schottky** test is used to obtain the built-in potential (V_{bi}) of PSCs devices, which is obtained by the following equation[9]:

$$\frac{1}{C^2} = \frac{2}{\varepsilon\varepsilon_0 qA^2N}(V_{bi} - V) \tag{4}$$

where C is the measured capacitance, A is the active area, V is the applied bias, ε is the static permittivity, ε_0 is the permittivity of free space, q is the elementary charge and N is the density of the free electrons.

The **trap density of states (tDOS)** can be deduced from the angular frequency-dependent capacitance using the equation[10]:

$$N_T E_\omega = -\frac{V_{bi}}{qW}\frac{dC}{d\omega}\frac{\omega}{k_B T} \tag{5}$$

where k_B is the Boltzmann constant, q is the elementary charge, T is the temperature, V_{bi} and W are obtained from the Mott-Schottky analysis, and the angular frequency ω is defined by the following relation:

$$E_\omega = k_B ln\frac{\omega_0}{\omega} \tag{6}$$

where ω_0 is the attempt-to-escape frequency. Combining equations S5 and S6, the tDOS level in different perovskite devices can be obtained.

***FF* loss** analysis is obtained using the following methods[11]:

$$\Delta FF\ loss = \Delta FF_{non-rad} + \Delta FF_{transport} \tag{7}$$

$$\Delta FF_{non-rad} = FF_{SQ-limi} - FF_{max} \tag{8}$$

$$\Delta FF_{transport} = FF_{max} - FF_{measured} \tag{9}$$

Here, $\Delta FF_{non-rad}$ represents the *FF* value attributed to non-radiative recombination losses, while $\Delta FF_{transport}$ represents the *FF* value associated with transport losses. Here, the $FF_{SQ-limit}$ is empirically set at 90.3% (for perovskites with a bandgap of 1.55 eV).[12, 13] The FF_{max} is obtained through the following empirical approximation formula, which emphasizes the maximum value of *FF* when the series resistance is zero and the shunt resistance is infinitely large, that is, when transport losses are not considered.[14, 15]

$$FF_{max} = \frac{\upsilon_{OC} - \ln(\upsilon_{OC} + 0.72)}{\upsilon_{OC} + 1} \tag{10}$$

$$\upsilon_{OC} = \frac{V_{OC}}{nk_B T/q} \tag{11}$$

n is the ideality factor of the perovskite solar cell, extracted from the V_{OC}-light intensity dependence. And k_B is the Boltzmann constant, q is the elementary charge, T is the temperature.

PLQY measurements. The excitation for PL measurement is carried out by using a 365nm laser to enter the integrating sphere through an optical fiber. By irradiating a 0.1 cm^2 perovskite solar cell under short circuit and matching the current density with J_{SC} under a solar simulator, the laser intensity was adjusted to 1 solar equivalent intensity. The quasi Fermi level splitting (QFLS) of pure absorber layers and multilayer device stacks was calculated based on PLQY.[16] Comparing the QFLS in the absorption layer with and without a transport layer can quantify the non-radiative losses at the interface between the perovskite layer and the transport layer. To understand the origin of non-radiative recombination losses in the device, we calculated the QFLS of a series of samples using the following relationship between QFLS and PLQY[17]:

$$QFLS = kT \ln(\mathrm{PLQY}\frac{J_G}{J_{0,rad}}) \tag{12}$$

In equation (12), k represents the Boltzmann constant, T is set to 25°C, J_G is the generated current density, which is almost equal to J_{SC} in all cases. $J_{0,\,rad}$ is the composite current density of radiation in thermal equilibrium or darkness, obtained by overlapping with the blackbody spectrum at 300 K:

$$J_{0,rad} = \mathrm{q}\int EQE_{PV}(E)\phi_{bb}(E)\,dE \tag{13}$$

where[18]

$$\phi_{bb}(E) = \frac{2\pi E^2}{h^3\mathrm{c}^2}\frac{1}{[exp(E/k\mathrm{T})-1]} \approx \frac{2\pi E^2}{h^3c^2}exp(\frac{-E}{kT}) \tag{14}$$

$\phi_{bb}(E)$ is the blackbody spectrum at temperature T (of the solar cell), h is Planck's constant, c denotes the speed of light in vacuum. Finally, we calculate the radiative limit for the open-circuit voltage ($V_{oc,rad}$) via[19]:

$$V_{oc,rad} = \frac{\mathrm{kT}}{\mathrm{q}}\ln(\frac{J_{sc}}{J_{0,rad}} + 1) \tag{15}$$

The **incident photon-to-electron conversion efficiency (IPCE)**, **electroluminescence (EL)**, and **transient photovoltage (TPV)** tests were measured using an ARKEO platform from Cicci research Italy. IPCE was measured based on a 300 W Xenon lamp. It was recorded as a function of wavelength under a constant white light bias of approximately 5 mW/cm^2 supplied by an array of white light emitting diodes.

A non-reflective metal mask with an aperture area of 0.1 cm^2 was used to cover the active area of the device to avoid light scattering through the sides.

The **Photothermal deflection spectroscopy (PDS)** measurements were carried out with a 1 kW Xe arc lamp and a 0.25 m grating monochromator as the tunable light source. The pump beam was modulated at 13 Hz. The probe laser was directed parallel to the sample from a Uniphase HeNe laser. A quadrant cell (United Detector Technology) was used as the position sensor for monitoring the photothermal deflection signal of the probe beam. The output of the detector was fed into a lock-in amplifier (Stanford Research, Model SR830).

The ***J-V* sweep** was performed using a Keithley 2400 source meter under simulated AM 1.5G one sun illumination (100 mW/cm^2) using a solar simulator (Oriel Sol 3A class AAA) equipped with a 450 W xenon lamp (Newport 6280NS). Typically, the devices are measured in reverse scan (1.2 V → 0 V, step 0.02 V) and forward scan (0 V → 1.2 V, step 0.02 V). All the devices are measured without pre-conditioning, such as light-soaking, and without applying a bias voltage. **Dark *J-V*** characteristics are based on the *J-V* characteristics with the light source turned off to perform the dark condition tests.

All stability tests were conducted without encapsulation. To ensure accurate results, the aging stability of unencapsulated perovskite films and perovskite solar cells were carefully monitored in sealed boxes, with strict control over the humidity air conditions required for corresponding aging. For the MPP tests of unencapsulated perovskite solar cells using the ISOS-L-1I[20] standard measurement conditions, we used white LED under N_2 conditions at room temperature. To capture precise data, *MPPT* were performed every 5 seconds, with recordings taken every 5 minutes.

A homemade LED light equipped with an AIDA LED panel with the spectrum showed in Figure S40 was used as the light source.

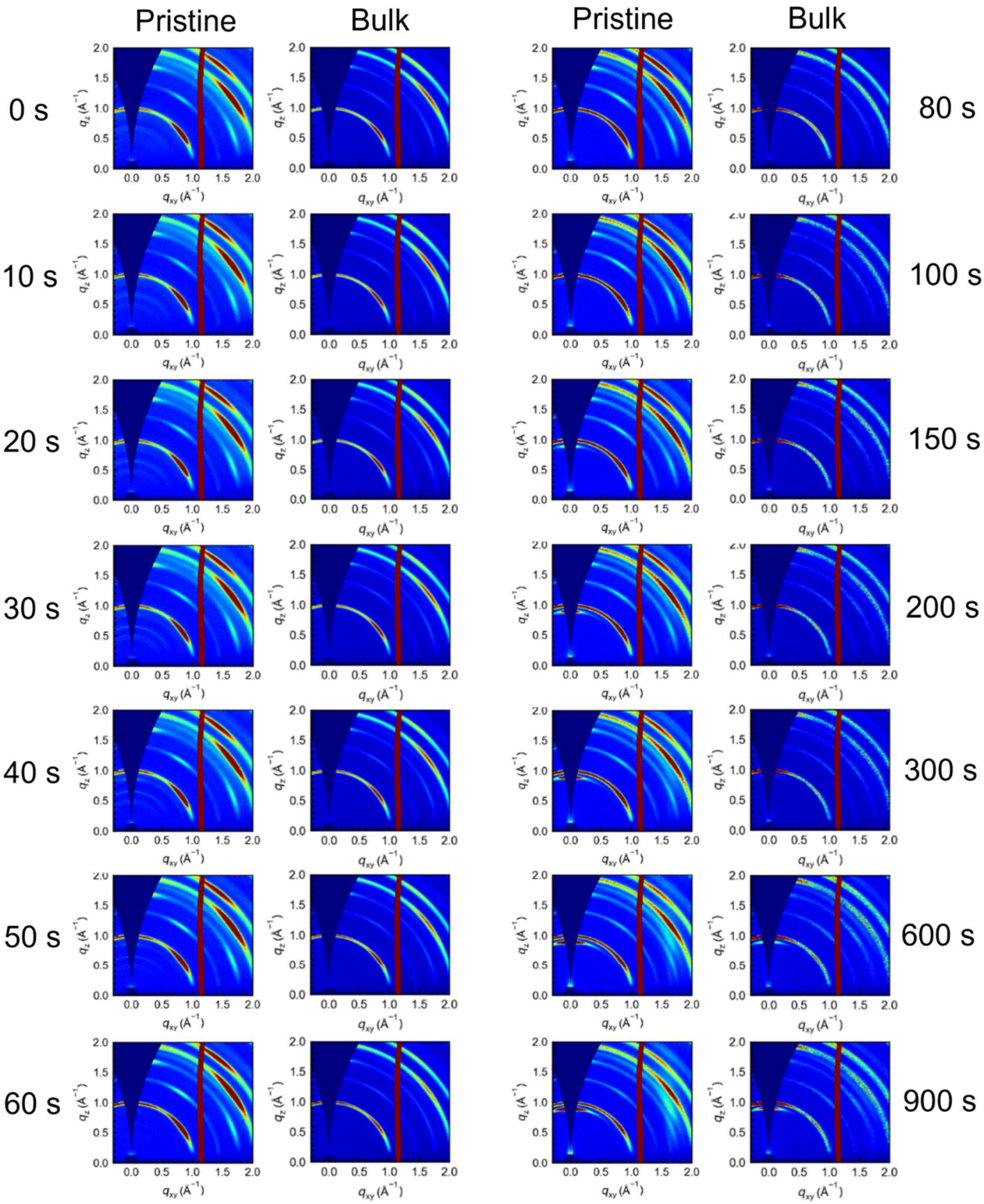

Figure S1. In-situ 2D-GIWAXS spectra of perovskite films of pristine PVK and PVK-PA (Bulk) during the annealing process (0-900 s).

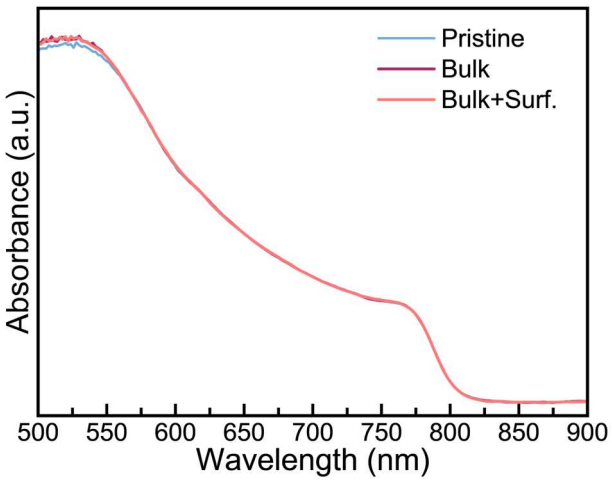

Figure S2. UV-vis absorption spectra of the pristine PVK, PVK-PA (Bulk), and PVK-PA (Bulk+Surf.) films.

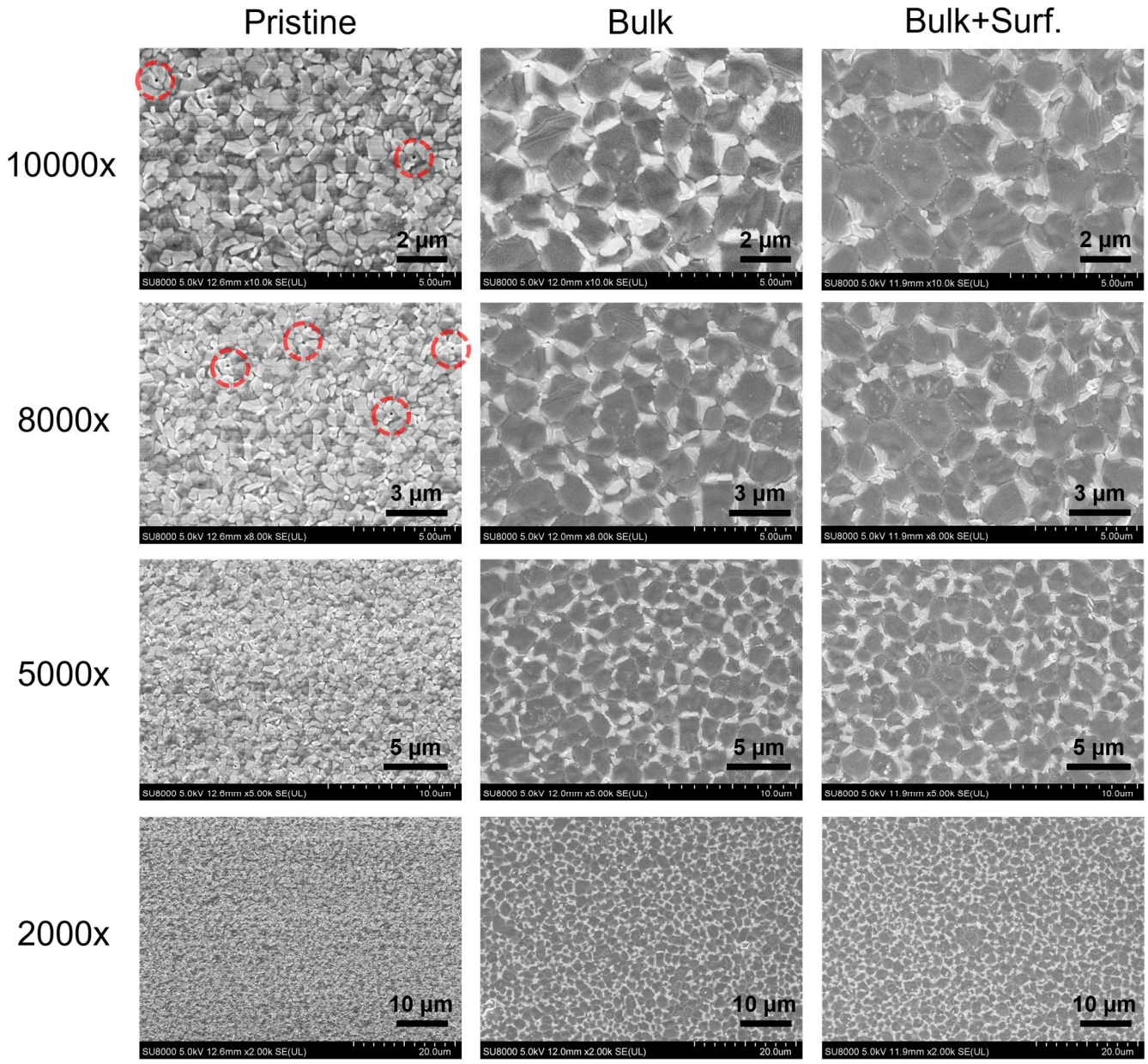

Figure S3. SEM images of perovskite films of pristine PVK, PVK-PA (Bulk) and PVK-PA (Bulk+Surf.) at 10000x, 8000x, 5000x and 2000x magnification (the red circle indicates the pinhole position).

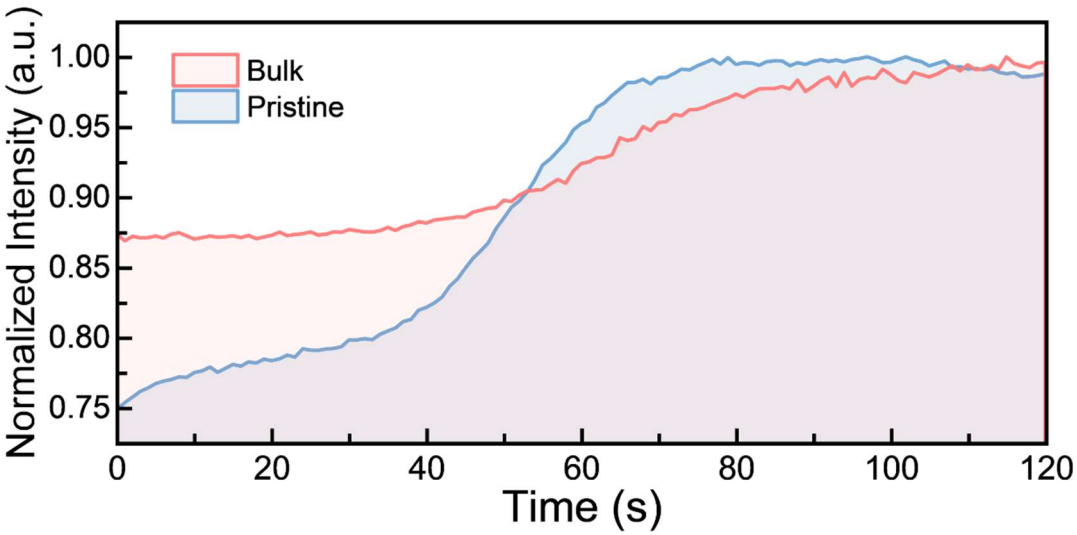

Figure S4. Time-resolved integrated peak area intensity of the (100) perovskite peaks for pristine PVK and PVK-PA (Bulk) (extracted from in-situ 2D-GIWAXS images).

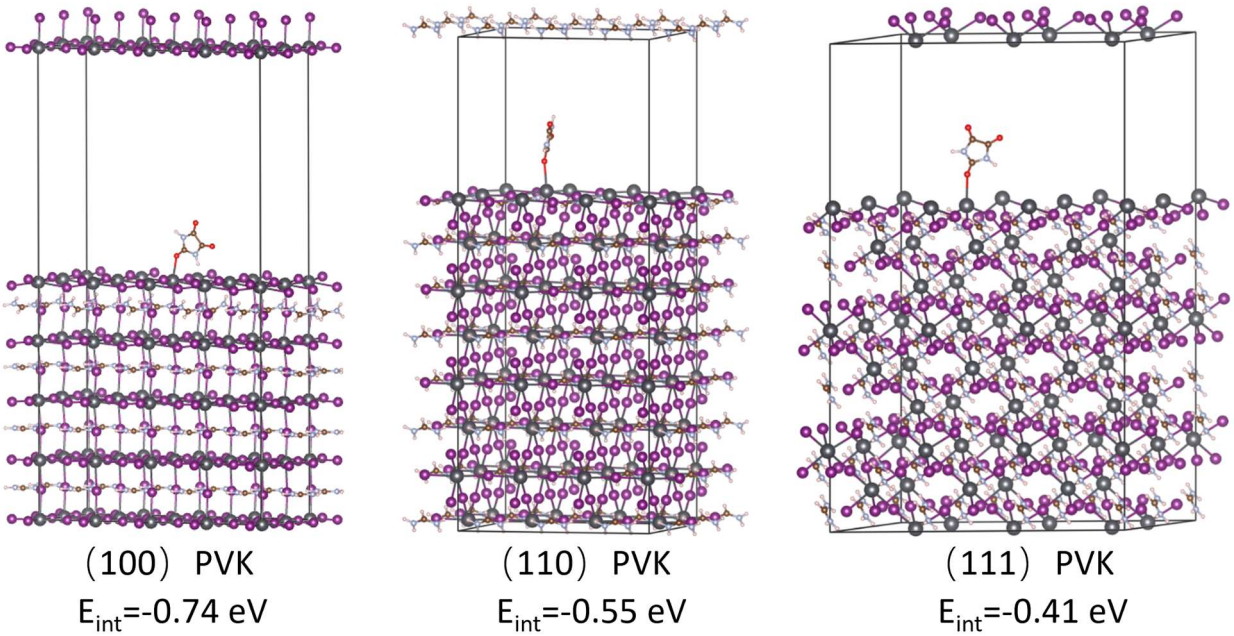

Figure S5. Theoretical calculation models of the binding of PA molecule to (a) 100, (b) 110, (c) 111 crystallographic planes of perovskite.

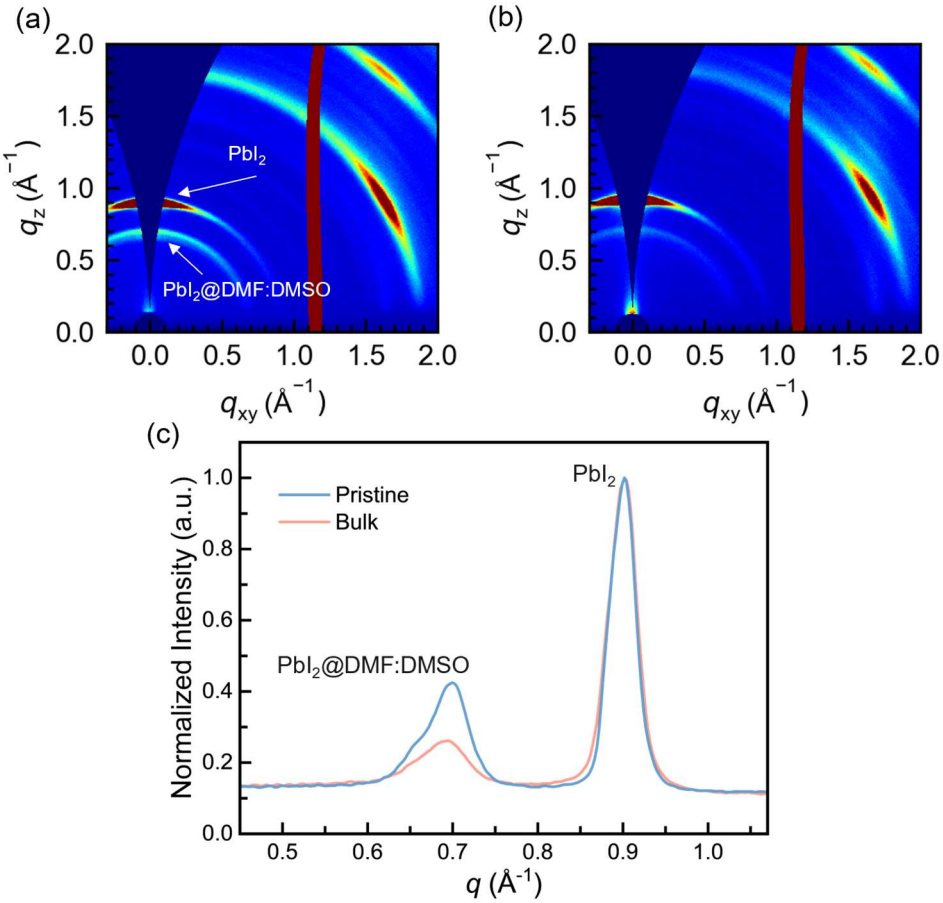

Figure S6. 2D-GIWAXS spectra of PbI_2 films of (a) pristine PbI_2 and (b) PbI_2-PA (Bulk). (c) 1D integral of the 2D-GIWAXS diffraction ring of pristine PbI_2 and PbI_2-PA (Bulk) films.

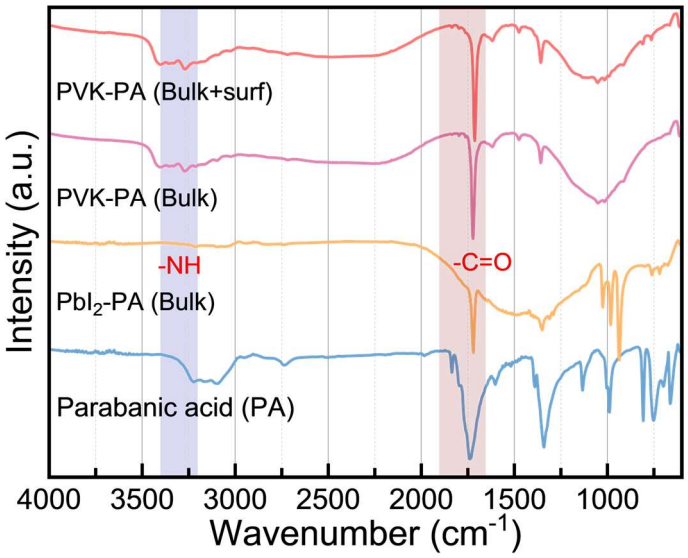

Figure S7. FTIR spectra of pure PA, PbI_2-PA (Bulk), PVK-PA (Bulk) and PVK-PA (Bulk+Surf.) films.

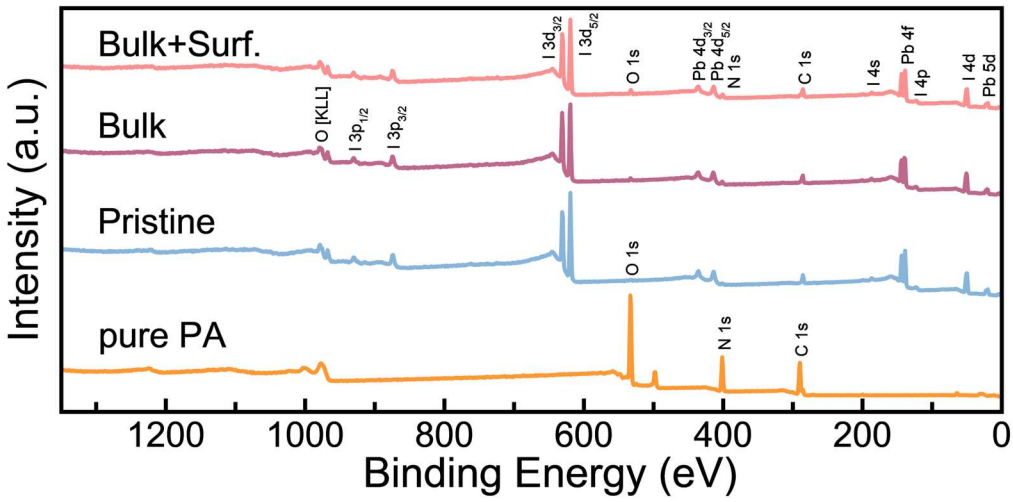

Figure S8. XPS full scan of pure PA, pristine PVK, PVK-PA (Bulk) and PVK-PA (Bulk+Surf.) films.

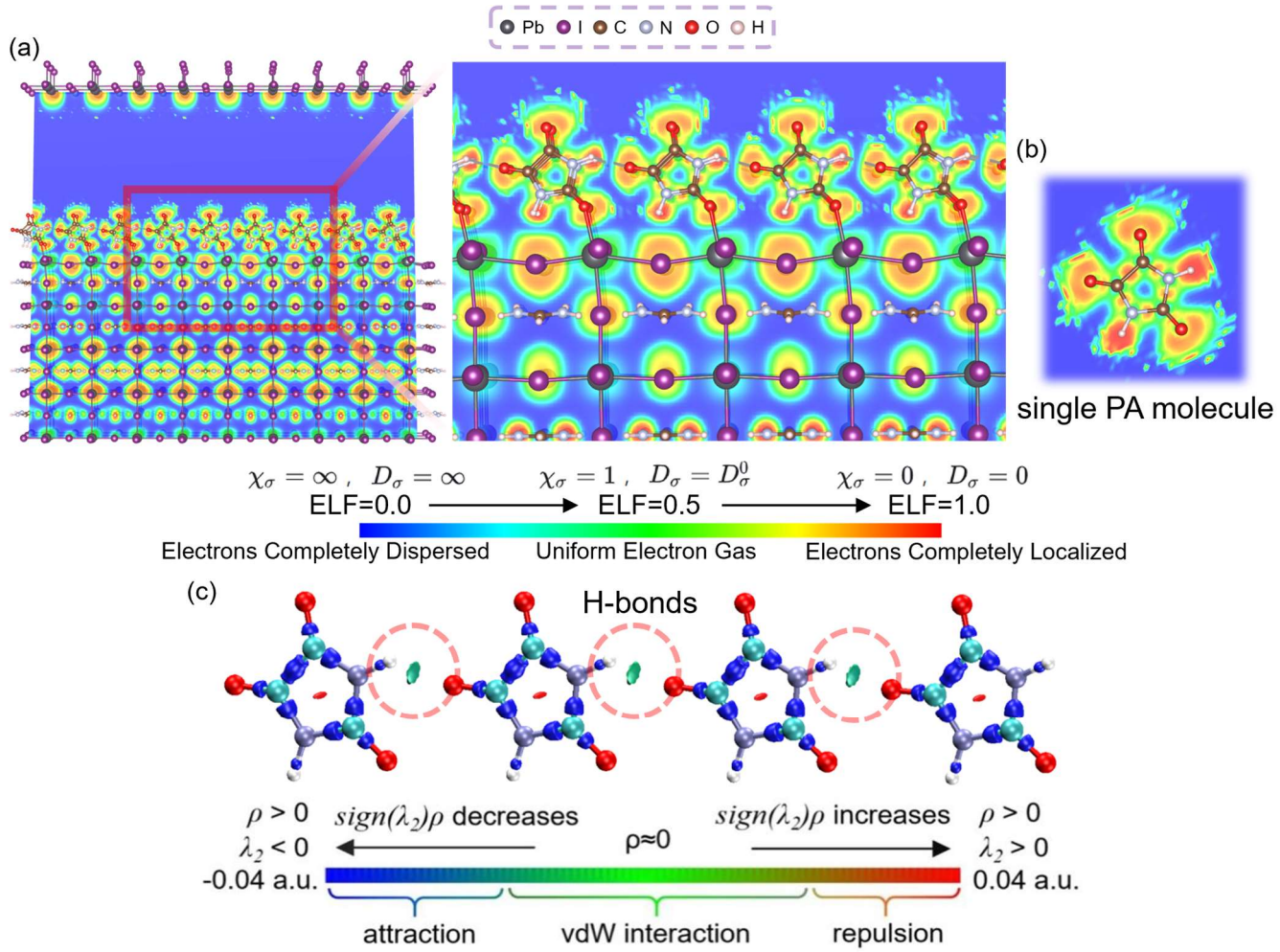

Figure S9. (a) Theoretically calculated ELF function image of lateral binding of PA on the surface of perovskite crystals. (b) ELF function image of a single PA molecule. (c) Theoretically calculated visualization image of IRI function of lateral binding of PA molecules.

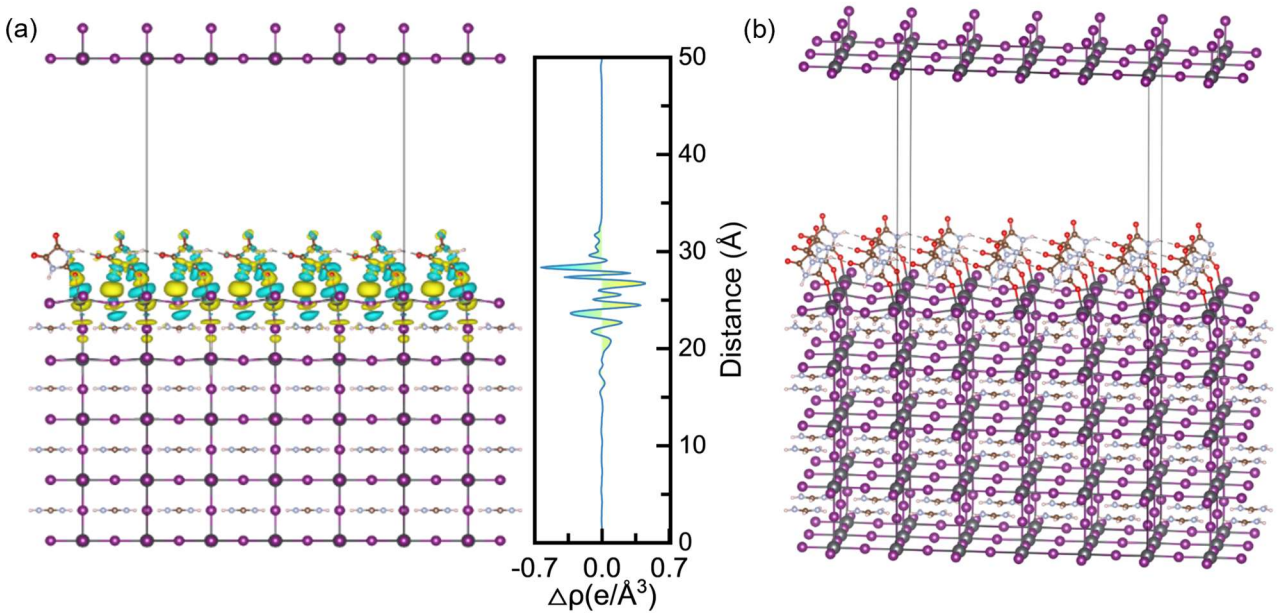

Figure S10. (a) Differential charge density image of PA lateral binding on the surface of perovskite crystal obtained by theoretical calculation. (b) Lateral binding image of PA on the surface of perovskite crystal obtained by theoretical calculation.

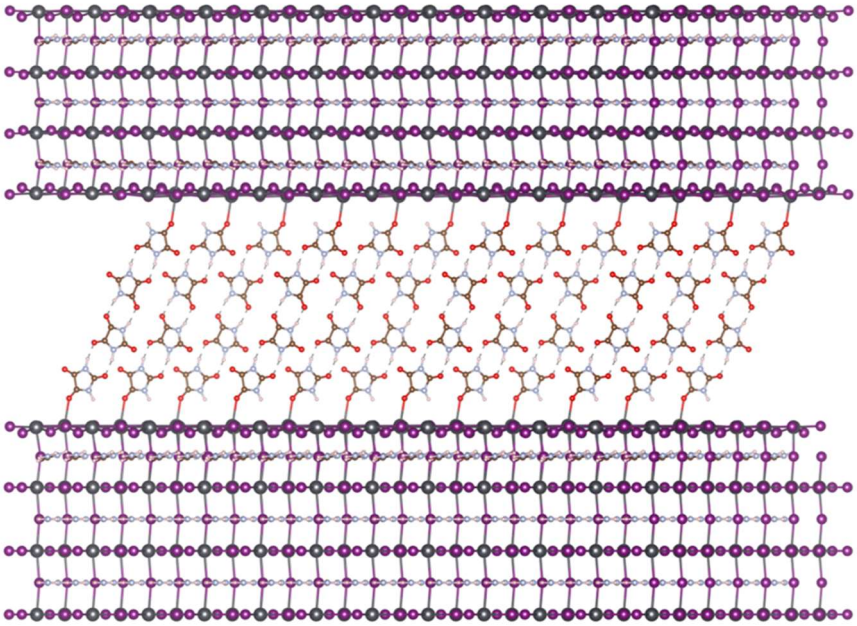

Figure S11. Schematic diagram of PA binding between two perovskite crystals. The unit structure calculated by DFT is shown in Fig. S12. The schematic diagram is obtained by expanding the unit structure and rotating the perspective for a better view.

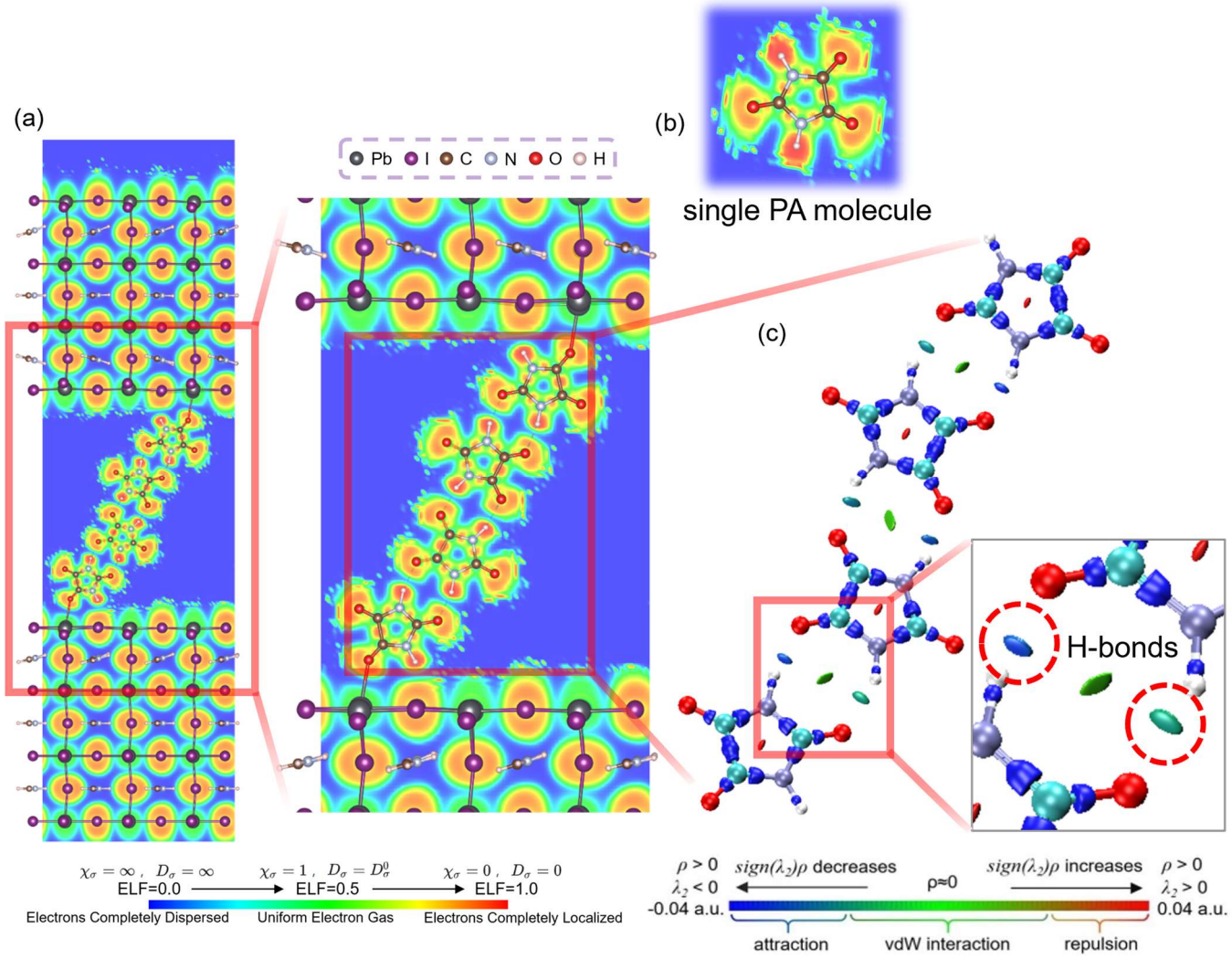

Figure S12. (a) Theoretically calculated ELF function image of PA binding between two perovskite crystals. (b) ELF function image of a single PA molecule. (c) Theoretically calculated IRI function visualization image of PA molecule longitudinal binding. The initial configuration of heterojunction structure optimization was obtained through quantum chemistry optimization of PA molecular chain structure.

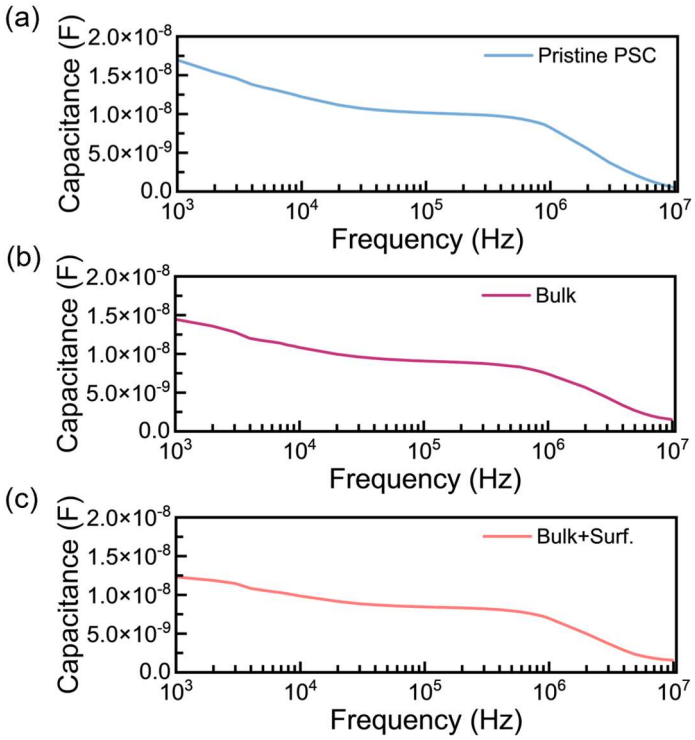

Figure S13. *C-f* curves of (a) pristine PSC, (b) PSC-PA (Bulk) and (c) PSC-PA (Bulk+Surf.).

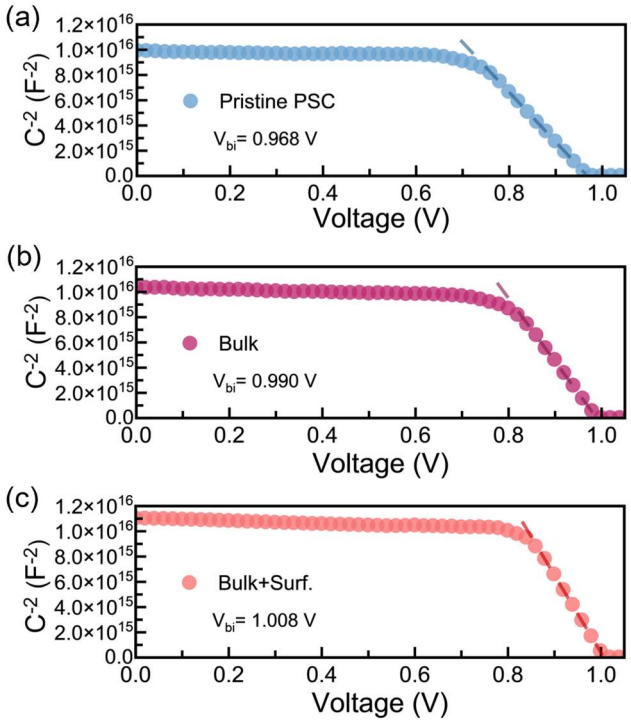

Figure S14. Mott-Schottky plots of (a) pristine PSC, (b) PSC-PA (Bulk) and (c) PSC-PA (Bulk+Surf.).

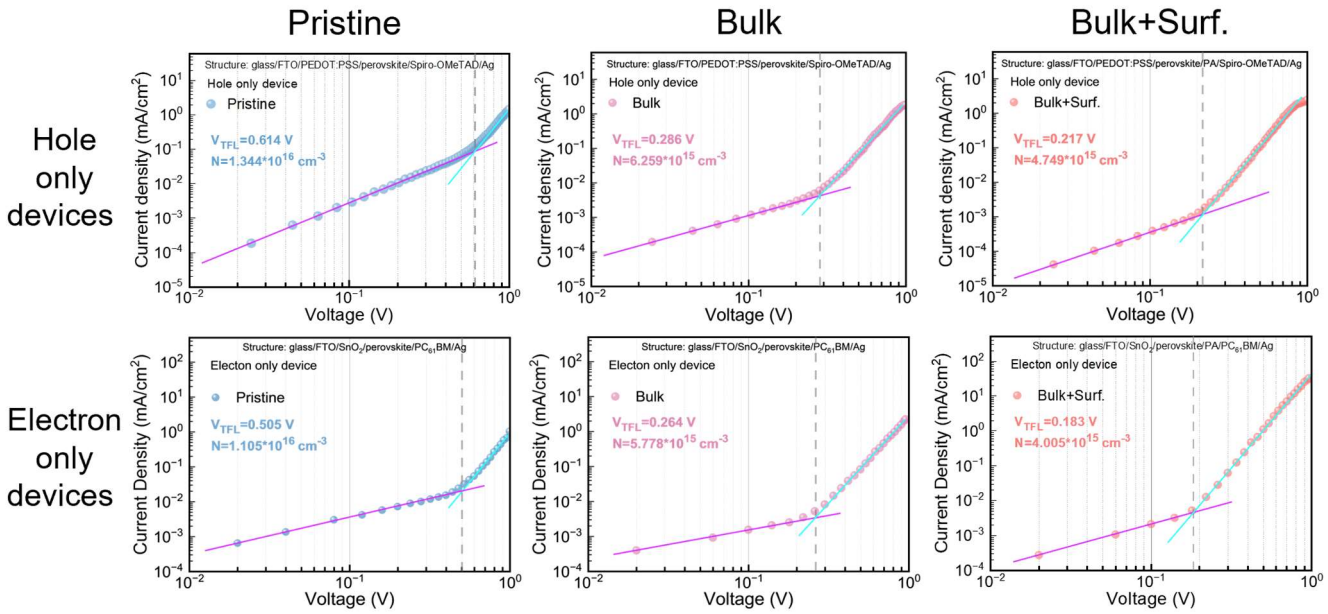

Figure S15. The hole-only SCLC measurements and the electron-only SCLC measurements. (N represents the density of defects)

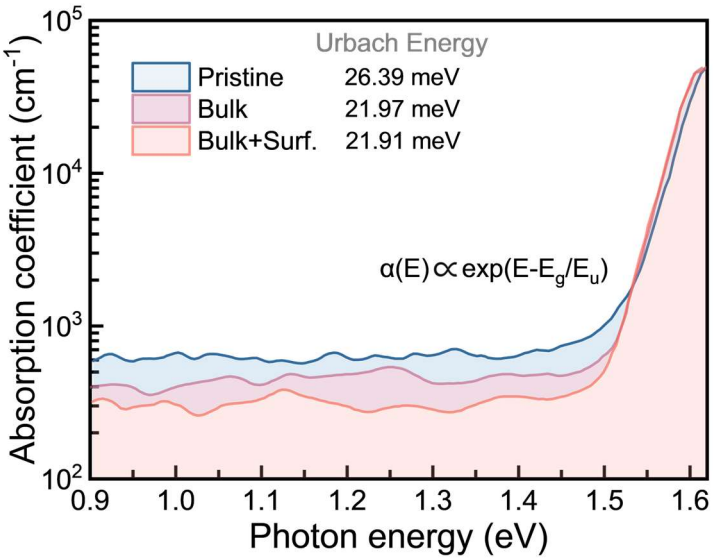

Figure S16. Photothermal deflection spectroscopy (PDS) of pristine PVK, PVK-PA (Bulk) and PVK-PA (Bulk+Surf.) films.

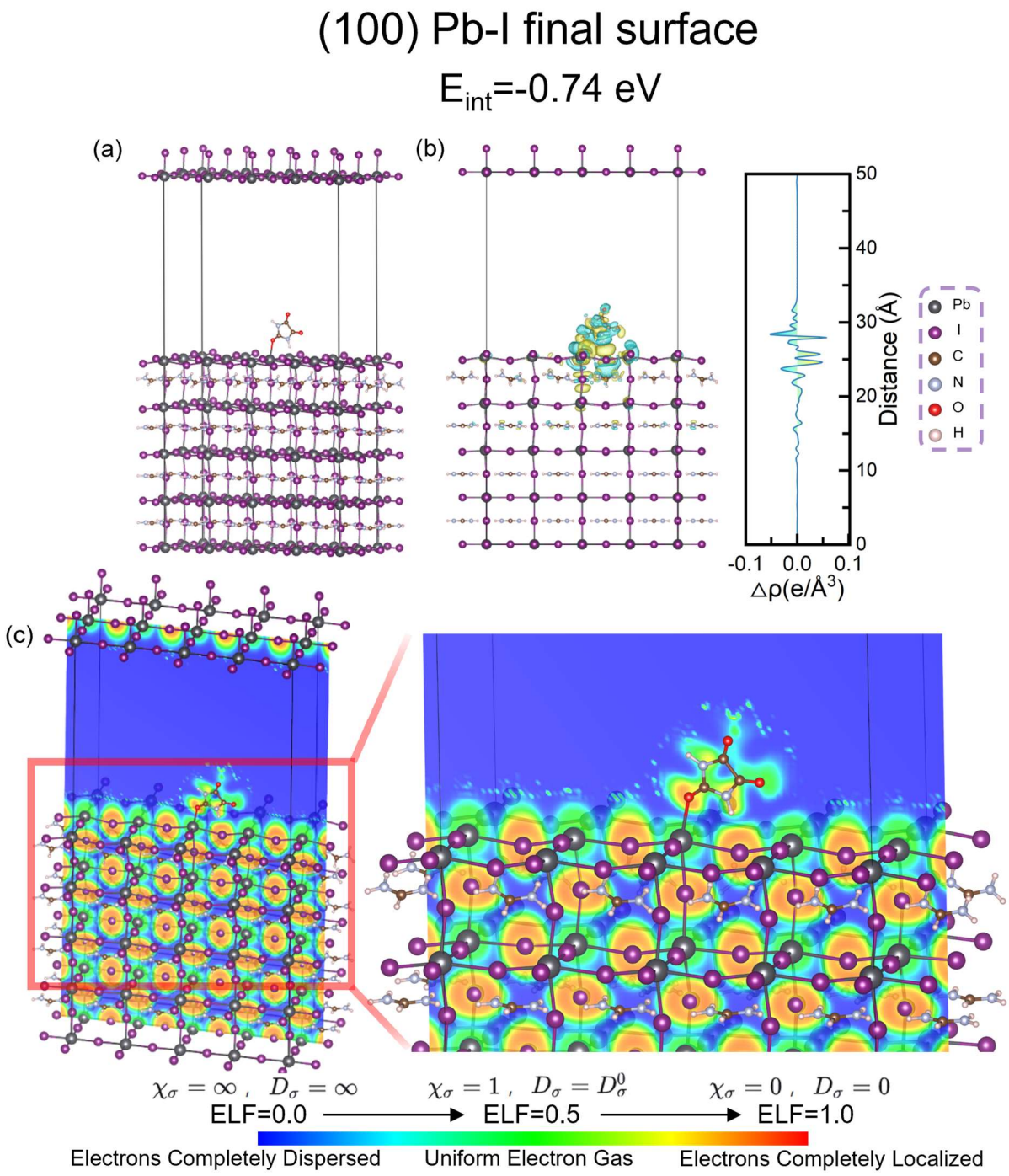

Figure S17. Theoretically calculated images of (a) the binding model of PA molecule with (100) Pb-I terminated perovskite surface, (b) the differential charge density, and (c) the ELF function images.

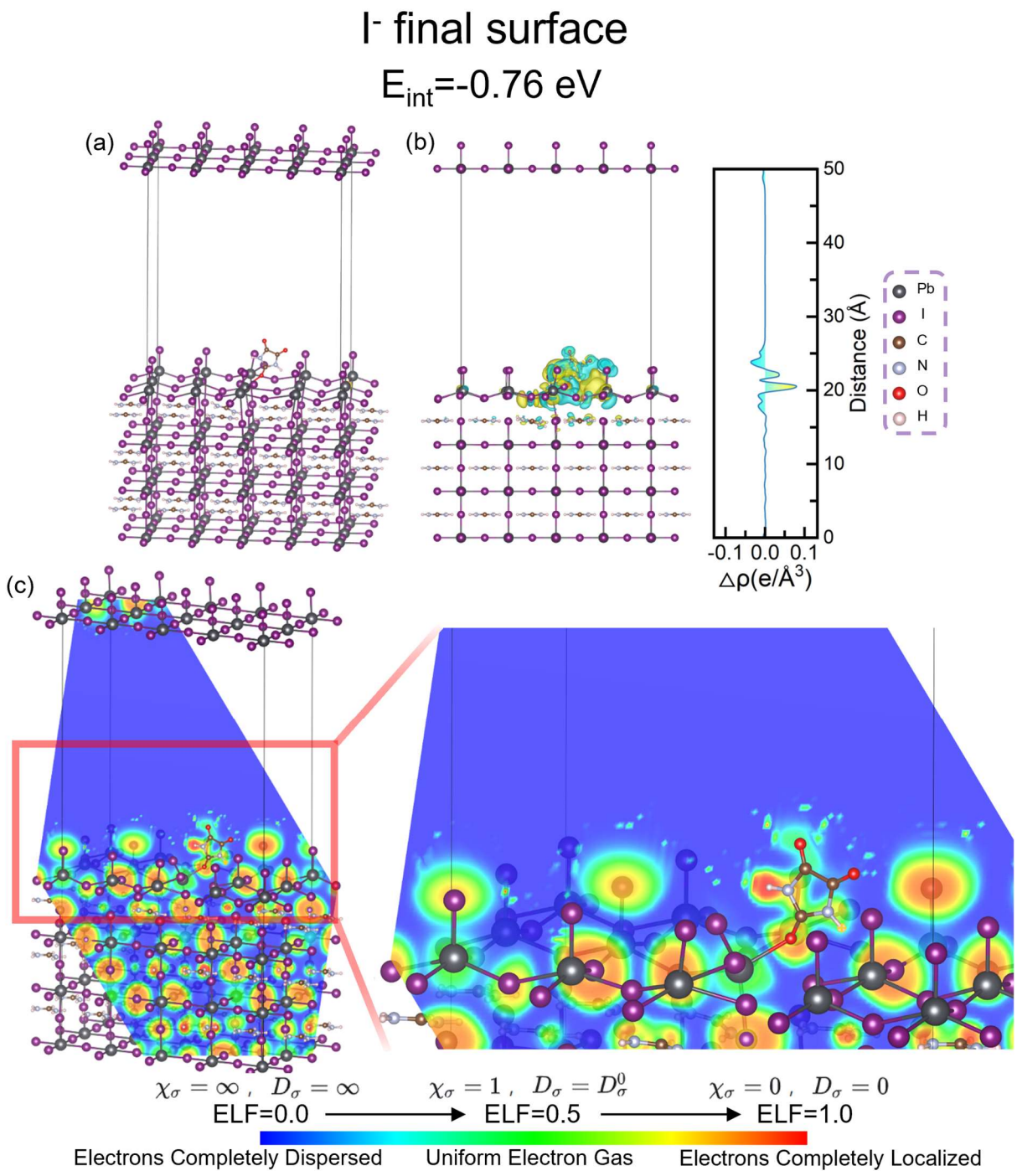

Figure S18. Theoretically calculated images of (a) the binding model of PA molecule with (100) perovskite surface (I^- terminated), (b) the differential charge density, and (c) the ELF function images.

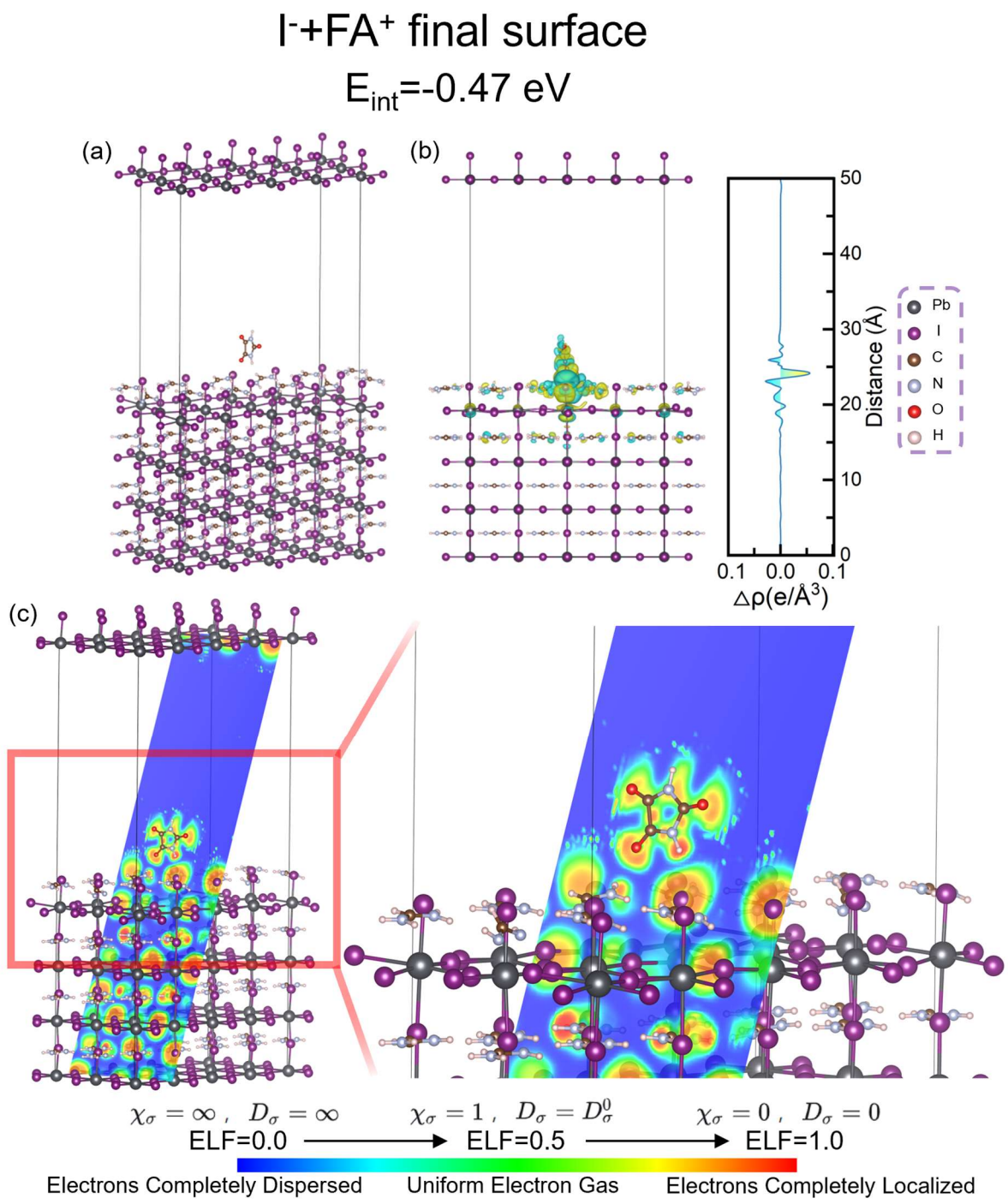

Figure S19. Theoretically calculated images of (a) the binding model of PA molecule with (100) I^-+FA^+ terminated perovskite surface, (b) the differential charge density, and (c) the ELF function images.

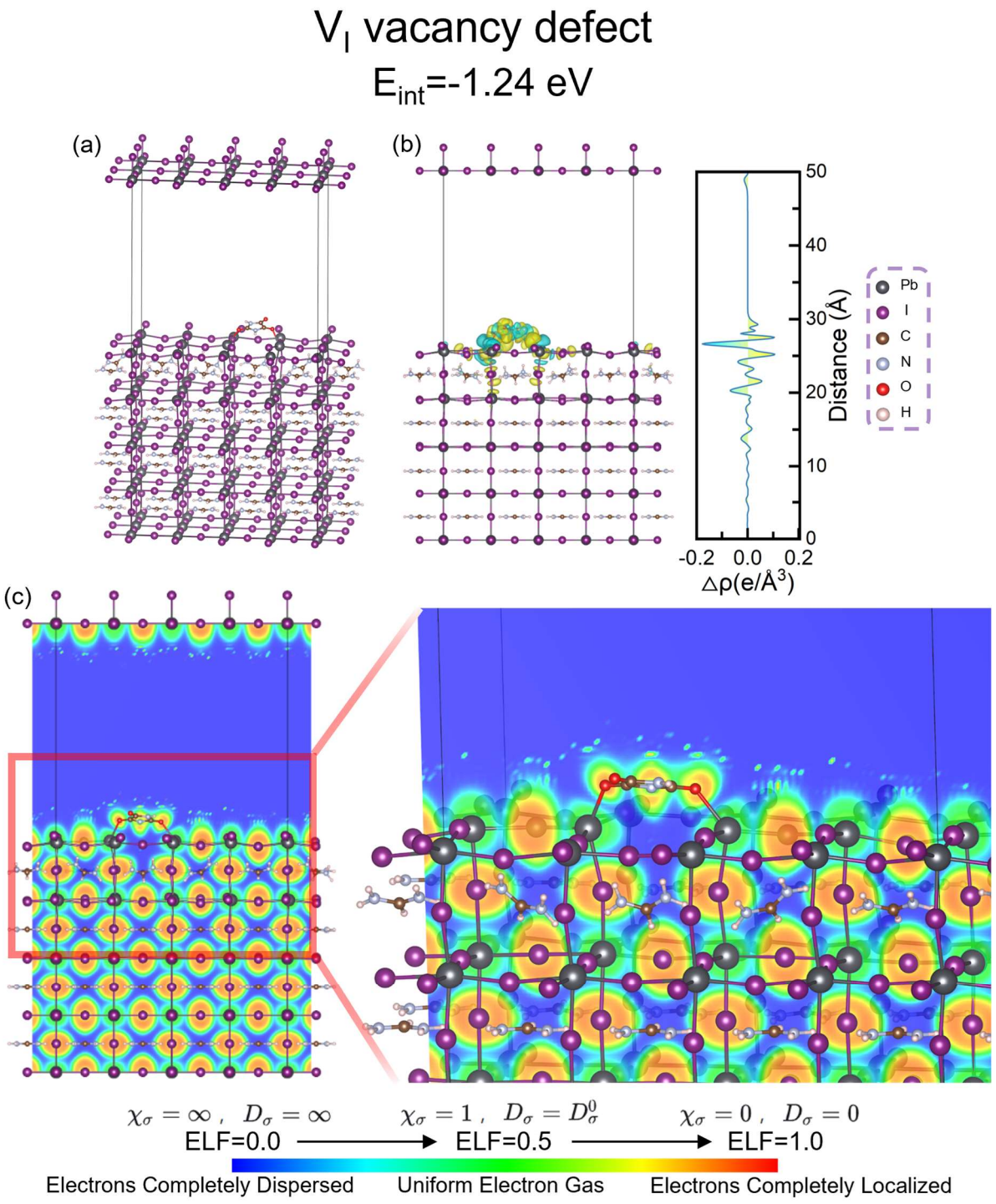

Figure S20. Theoretically calculated images of (a) the binding model of PA molecule with perovskite (with V_I vacancy defect), (b) the differential charge density, and (c) the ELF function images.

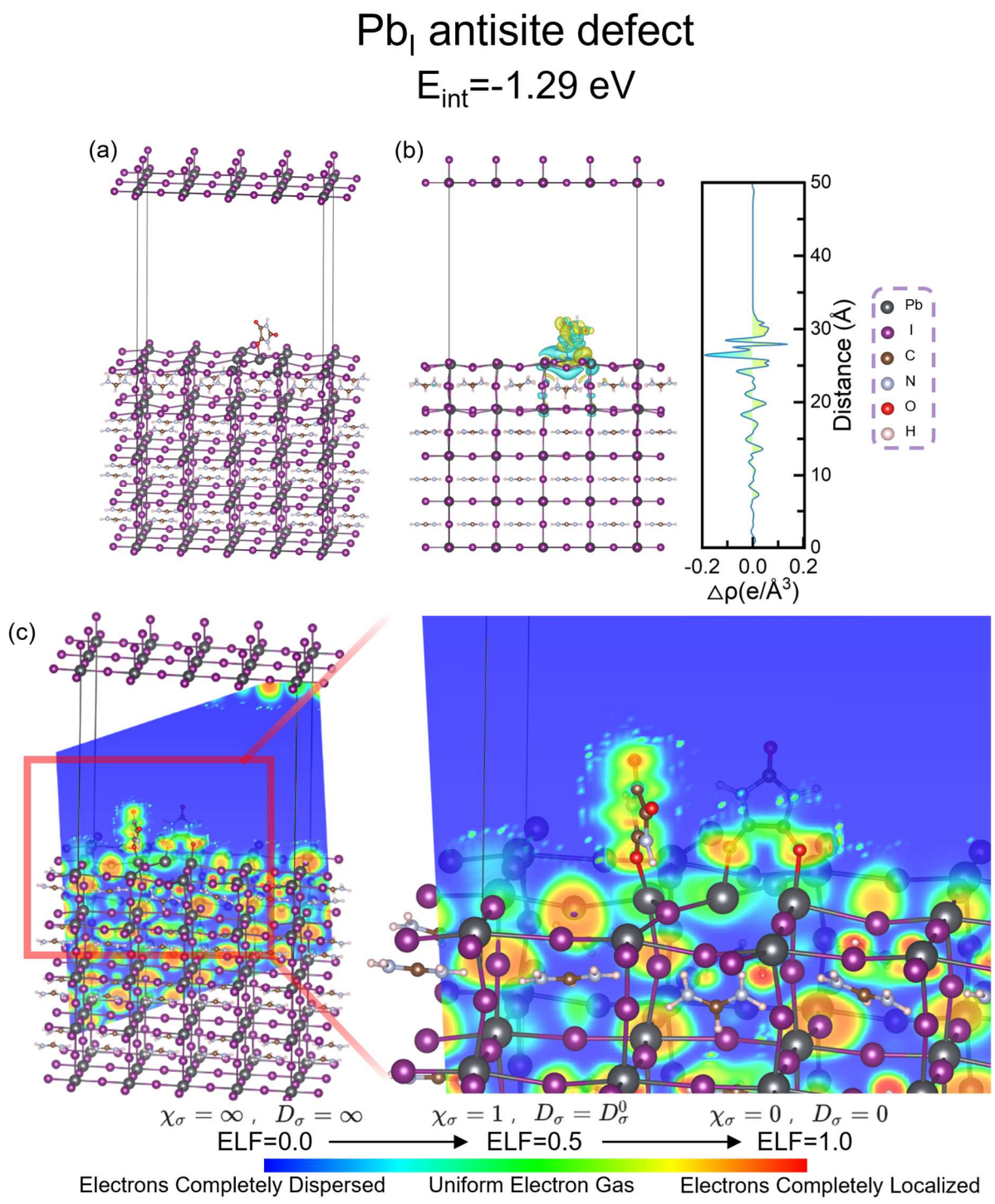

Figure S21. Theoretically calculated images of (a) the binding model of PA molecule with perovskite (with Pb_I antisite defect), (b) the differential charge density, and (c) the ELF function images.

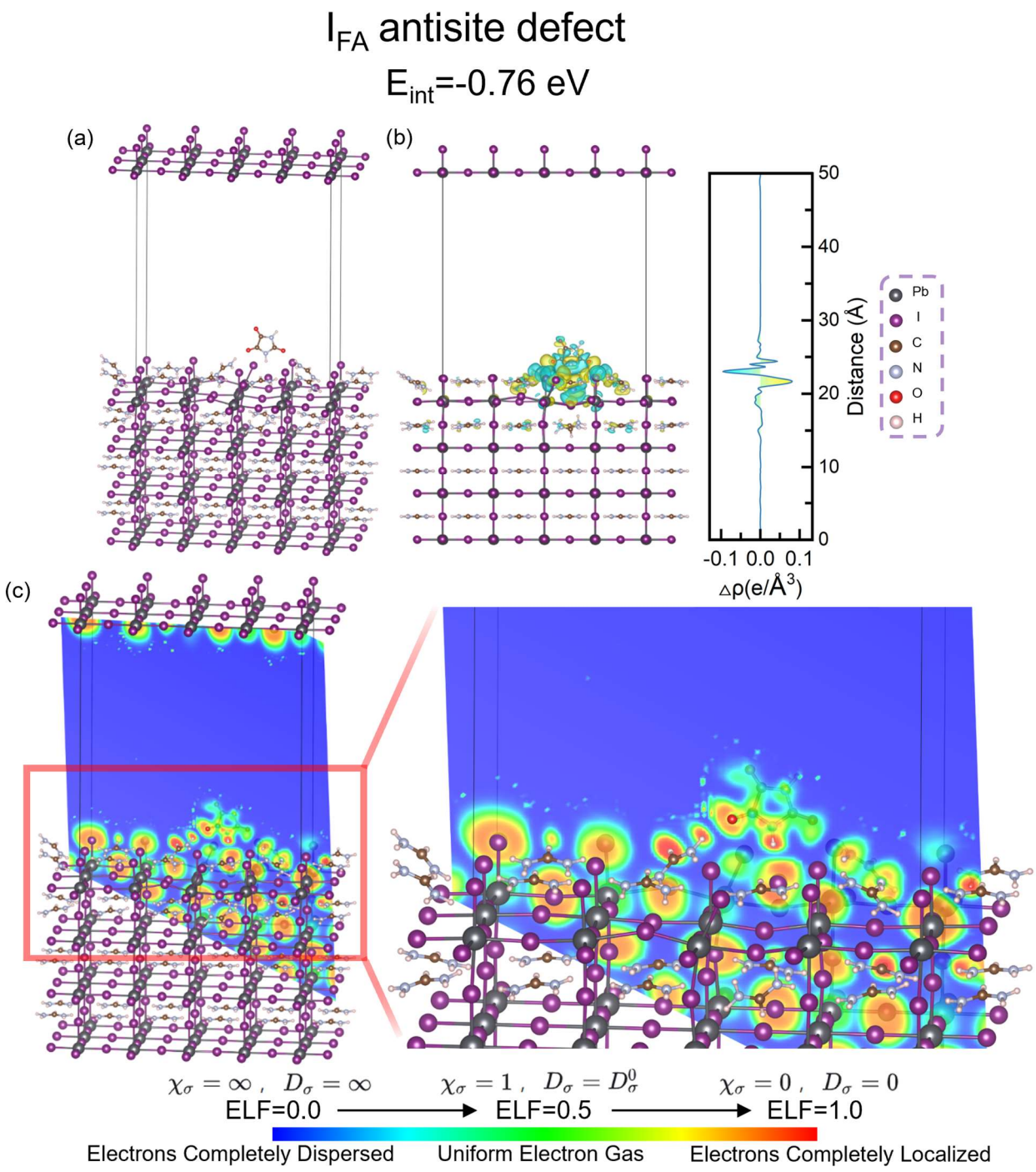

Figure S22. Theoretically calculated images of (a) the binding model of PA molecule with perovskite (with I_{FA} antisite defect), (b) the differential charge density, and (c) the ELF function images.

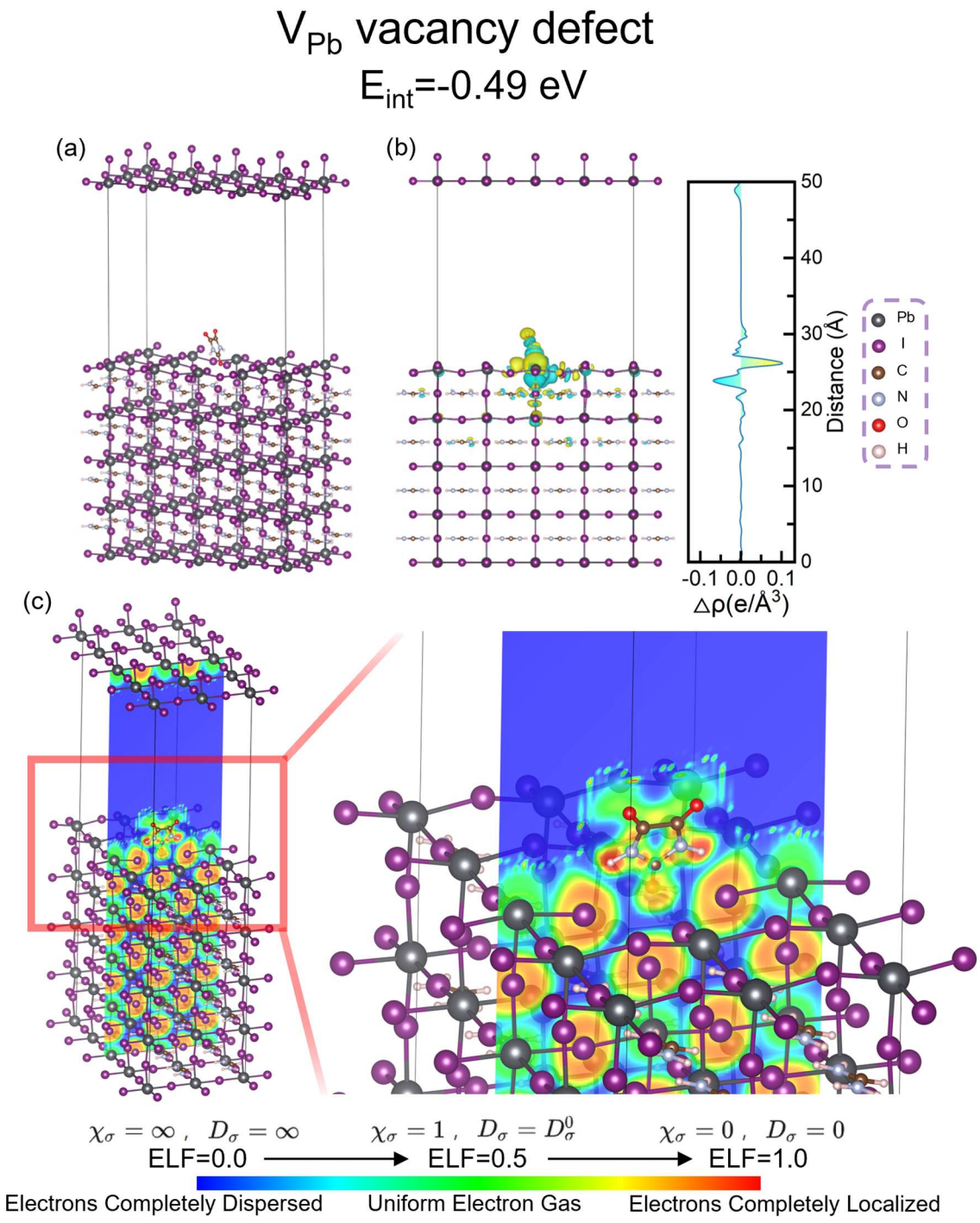

Figure S23. Theoretically calculated images of (a) the binding model of PA molecule with perovskite (with V_{Pb} vacancy defect), (b) the differential charge density, and (c) the ELF function images.

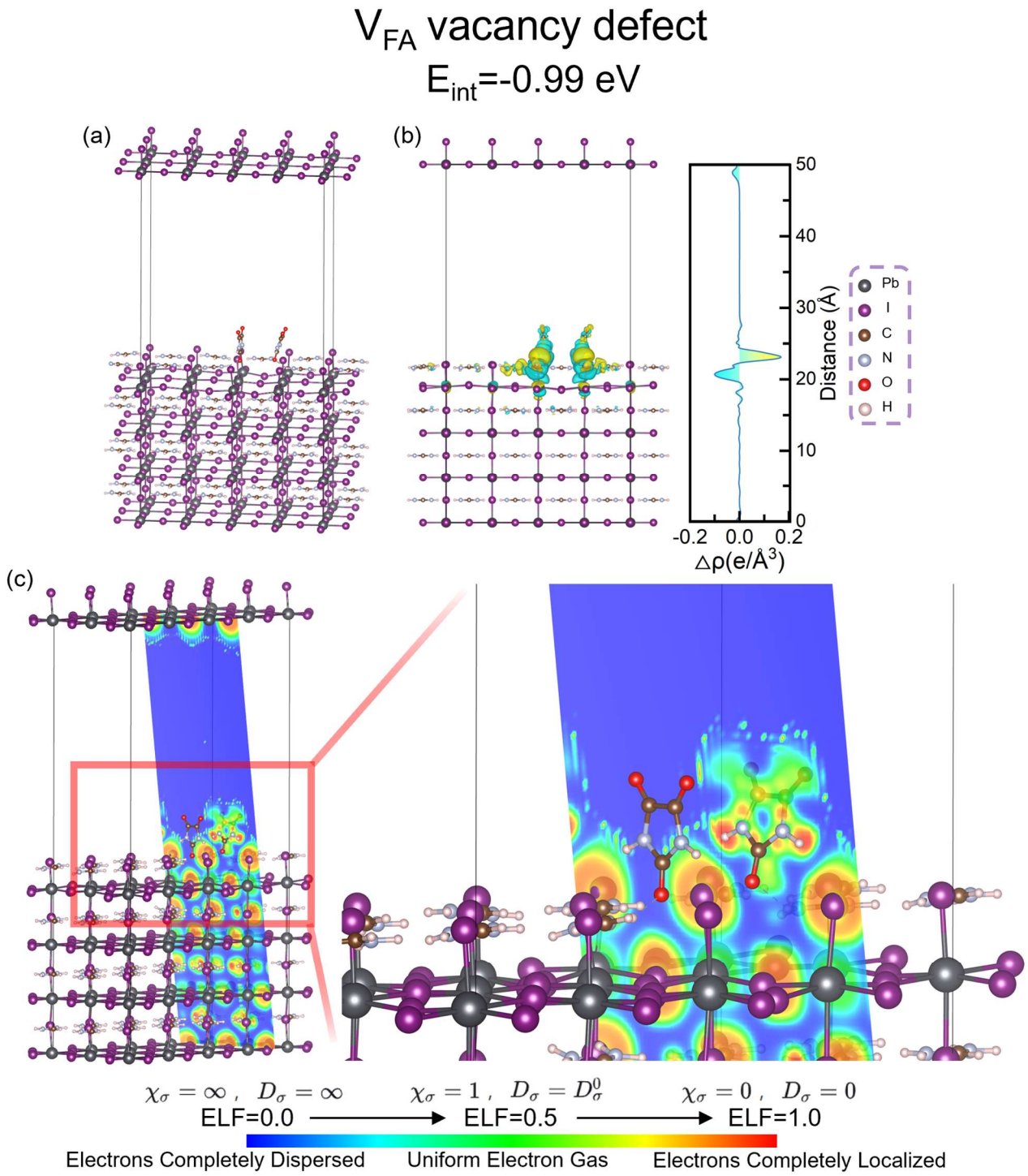

Figure S24. Theoretically calculated images of (a) the binding model of PA molecule with perovskite (with V_{FA} vacancy defect), (b) the differential charge density, and (c) the ELF function images.

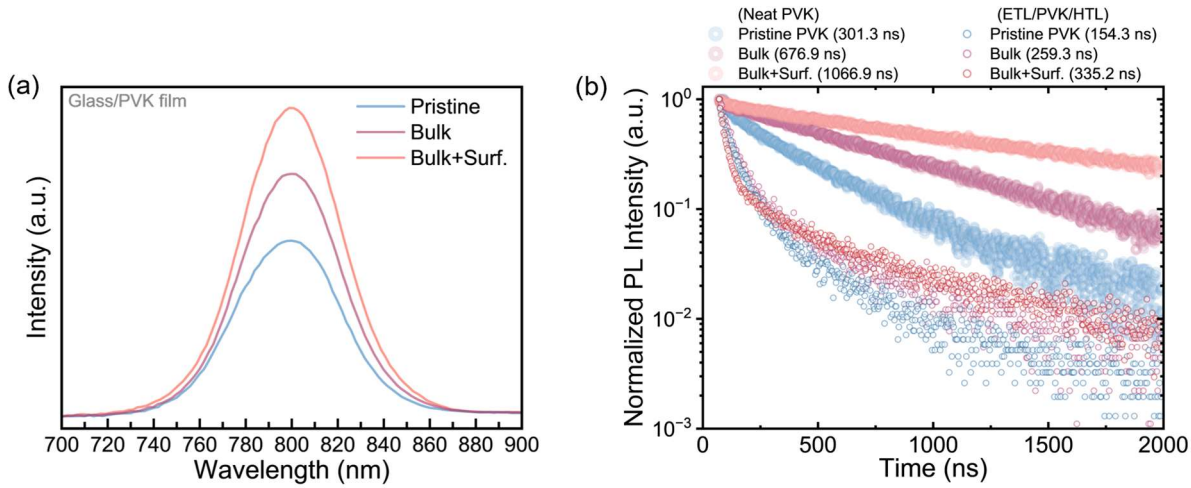

Figure S25. (a) Steady-state photoluminescence (PL) spectra. (b) Time-resolved PL (TRPL) spectra.

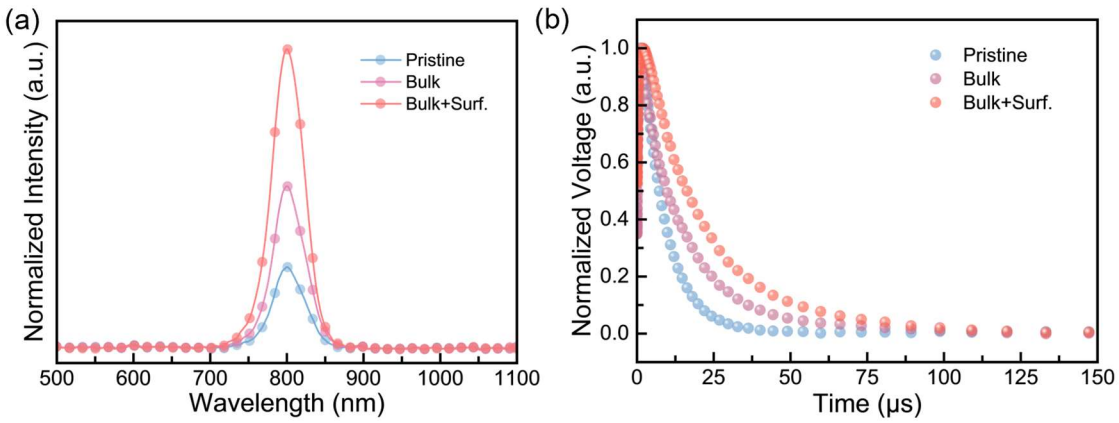

Figure S26. (a) Electroluminescence (EL) spectra. (b) Transient photovoltage (TPV) measurements.

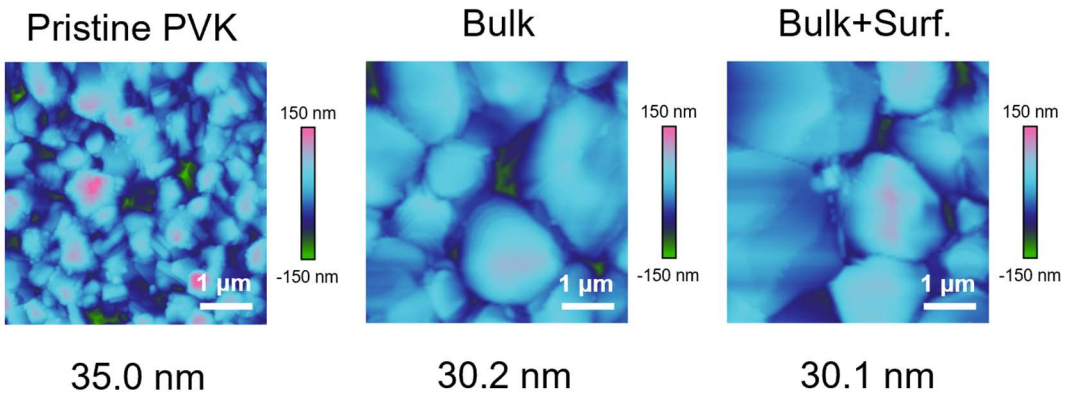

Figure S27. AFM images of pristine PVK, (b) PVK-PA (Bulk) and (c) PVK-PA (Bulk+Surf.) films.

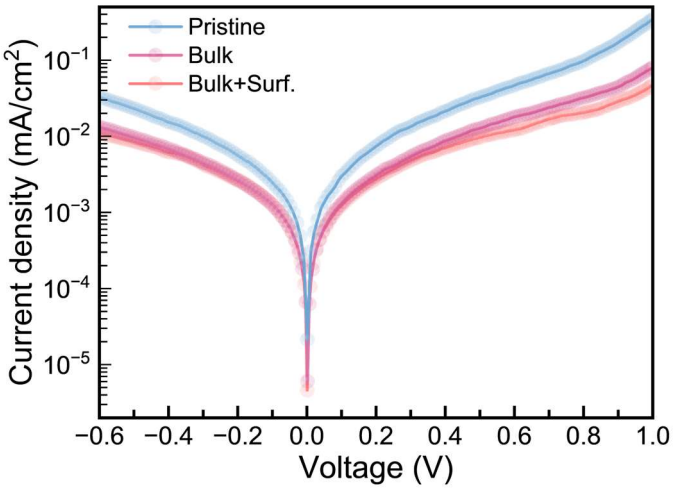

Figure S28. Dark *J-V* of pristine PSC, PSC-PA (Bulk) and PSC-PA (Bulk+Surf.).

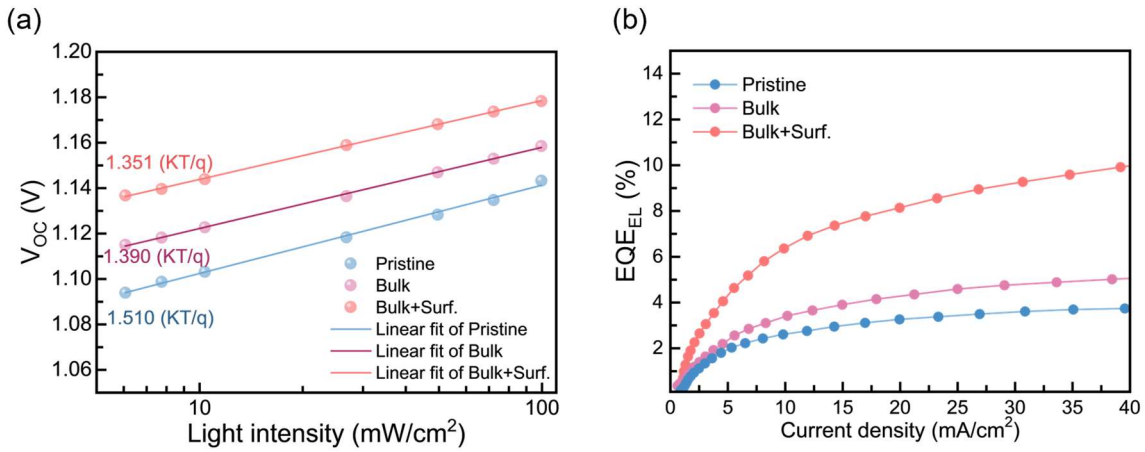

Figure S29. (a) V_{OC} dependence plots of pristine PSC, PSC-PA (Bulk) and PSC-PA (Bulk+Surf.). (b) EQE_{EL} plots of pristine PSC, PSC-PA (Bulk) and PSC-PA (Bulk+Surf.).

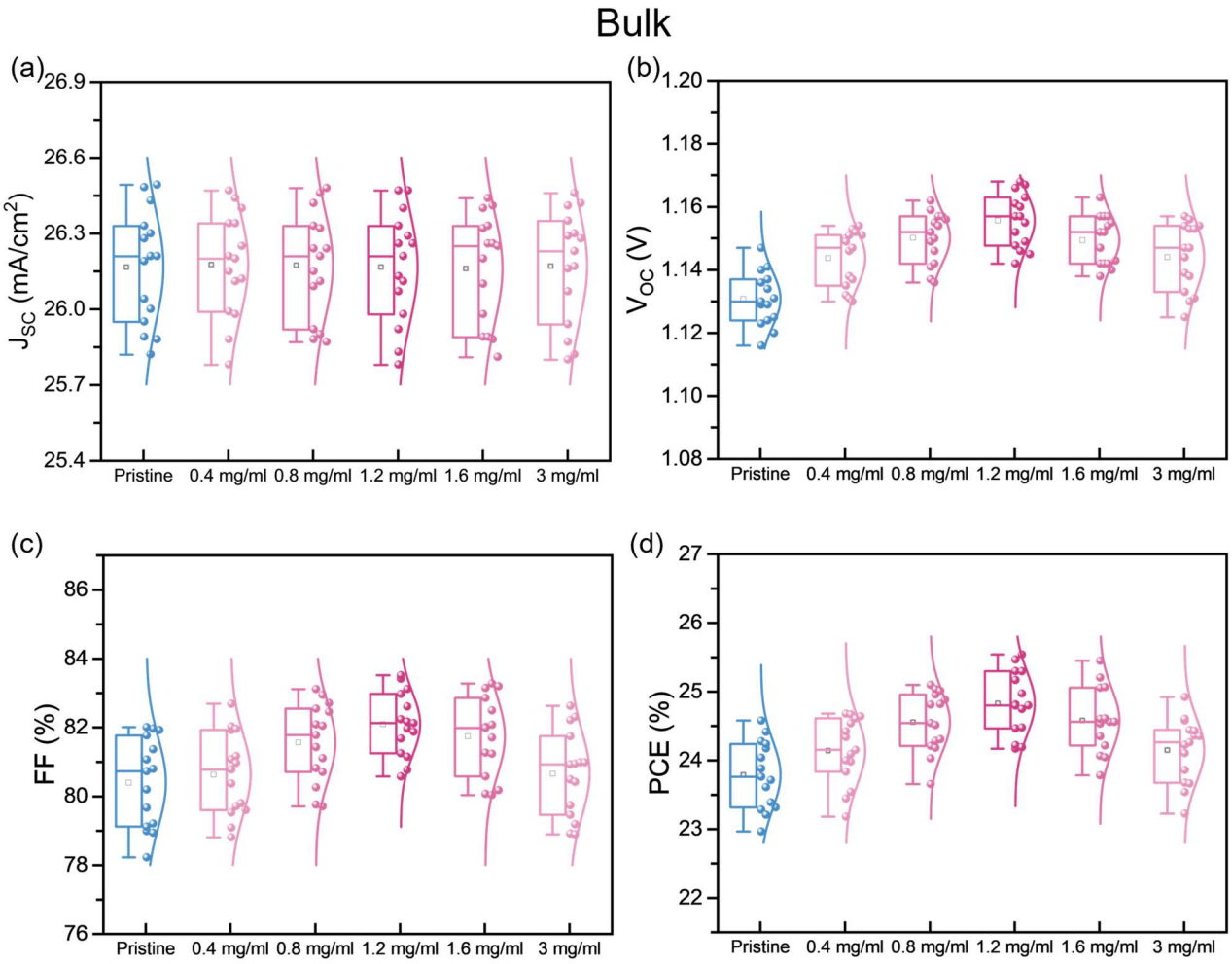

Figure S30. Photovoltaic parameters of (a) J_{SC}, (b) V_{OC}, (c) *FF* and (d) PCE for pristine PSCs and PSCs-PA (Bulk) (15 solar cells of each type).

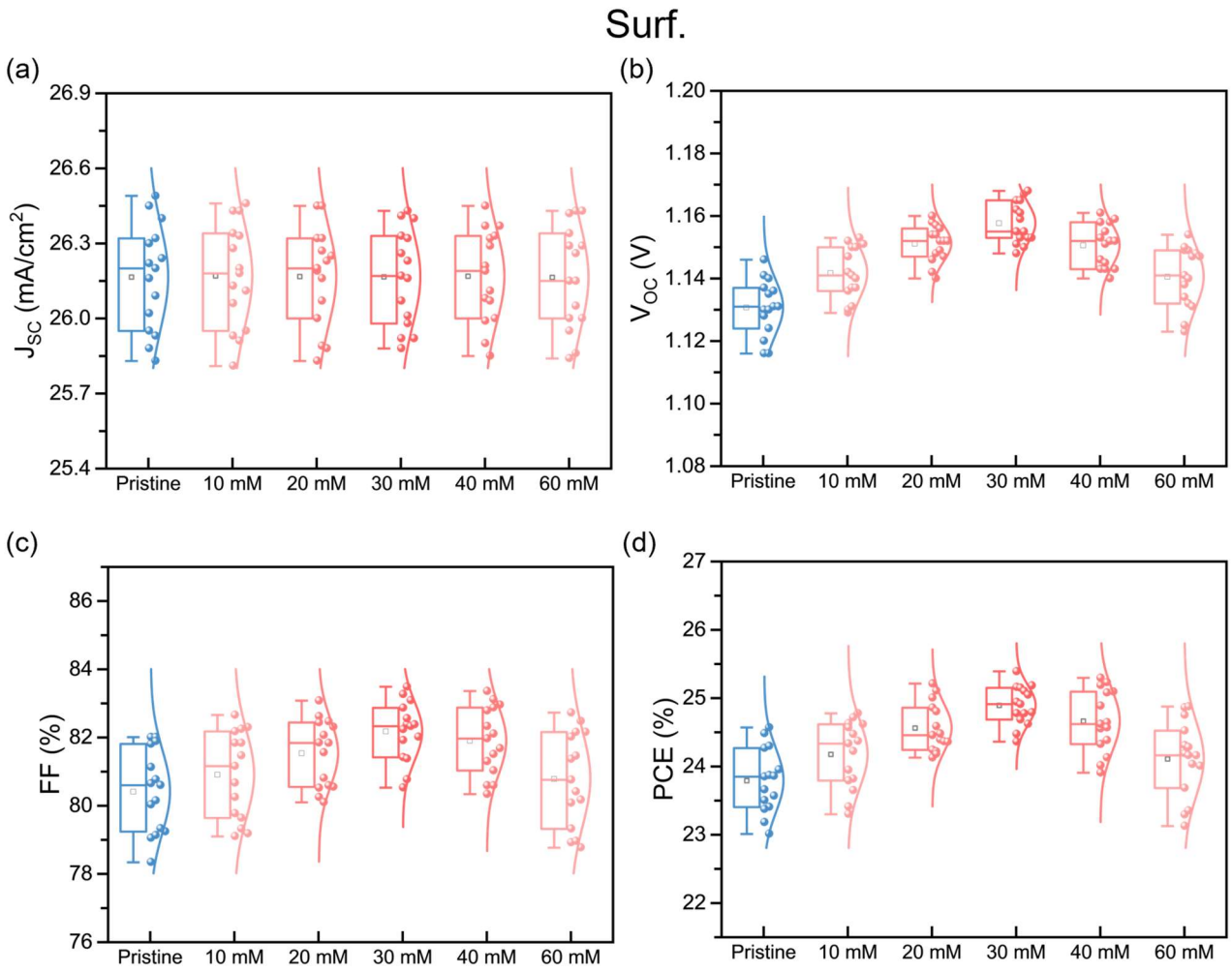

Figure S31. Photovoltaic parameters of (a) J_{SC}, (b) V_{OC}, (c) *FF* and (d) PCE for pristine PSCs and PSCs-PA (Surf.) (15 solar cells of each type).

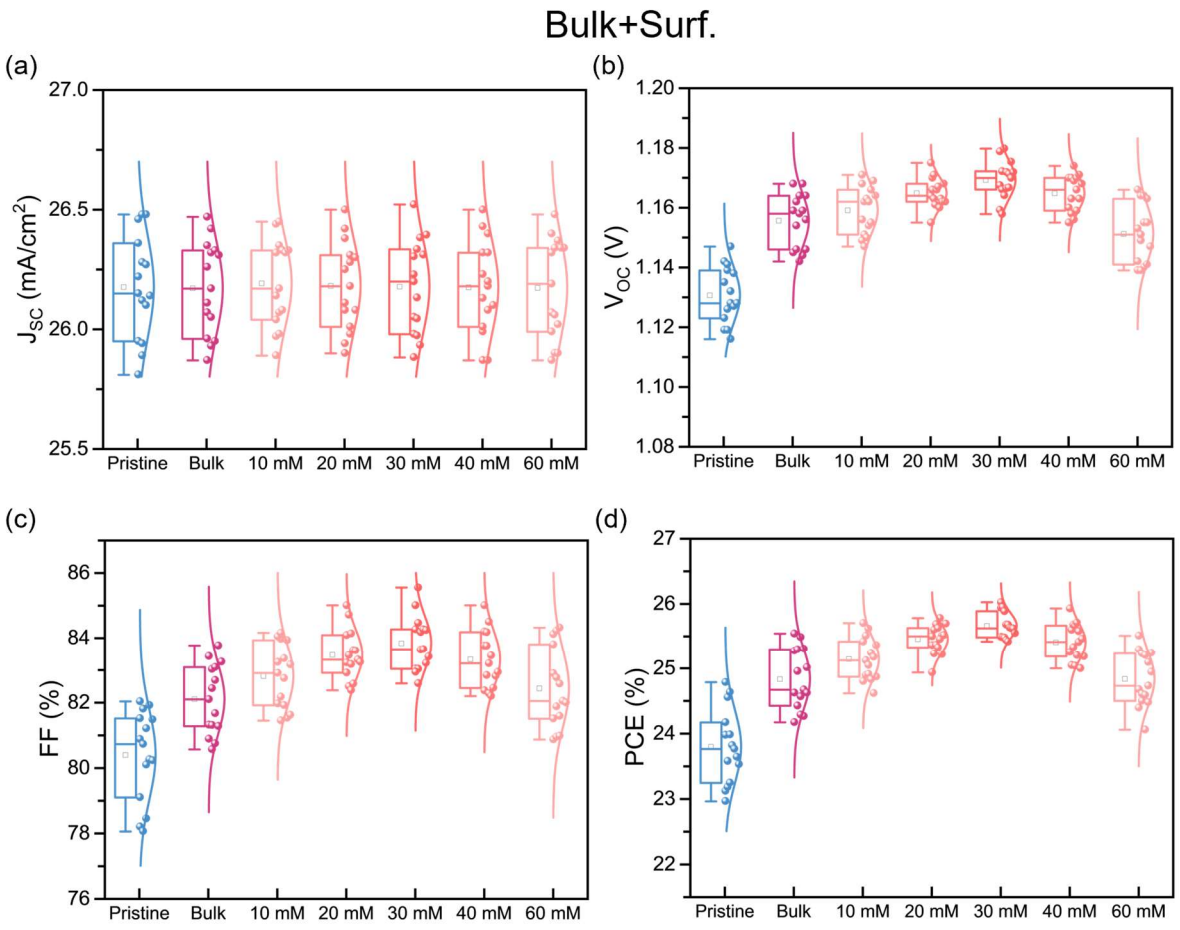

Figure S32. Photovoltaic parameters of (a) J_{SC}, (b) V_{OC}, (c) *FF* and (d) PCE for pristine PSCs and PSCs-PA (Bulk+Surf.) (15 solar cells of each type).

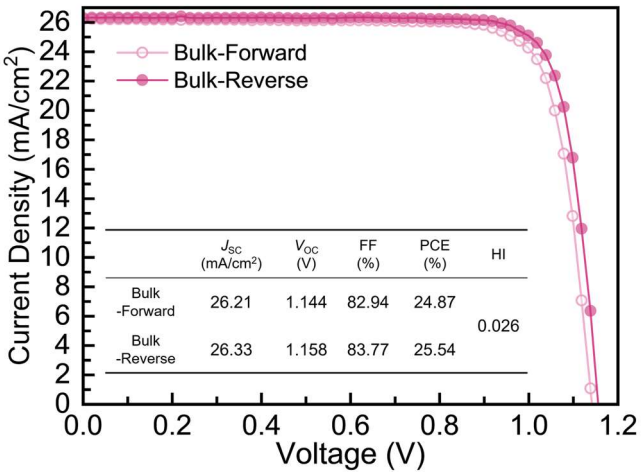

Figure S33. The *J-V* characteristics of the champion devices of PSC-PA (Bulk) scanned in the forward and reverse voltage directions.

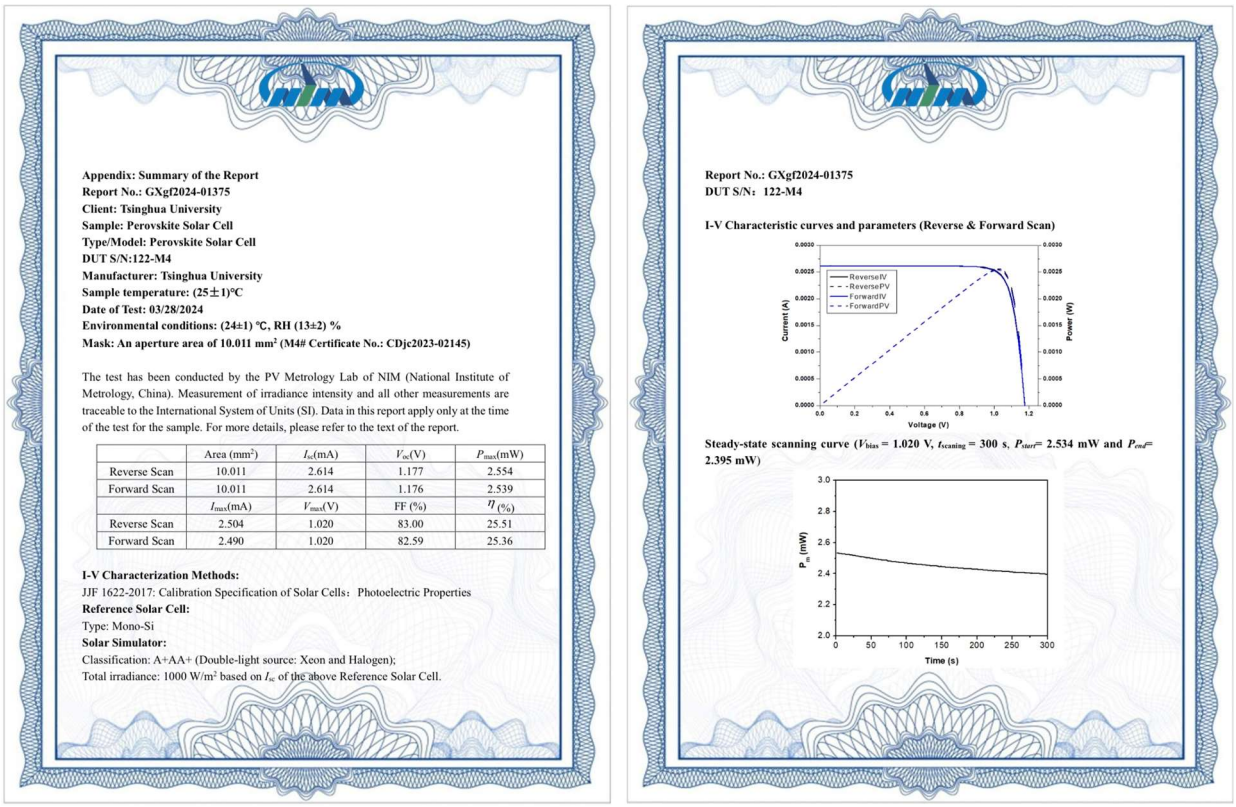

Appendix: Summary of the Report
Report No.: GXgf2024-01375
Client: Tsinghua University
Sample: Perovskite Solar Cell
Type/Model: Perovskite Solar Cell
DUT S/N:122-M4
Manufacturer: Tsinghua University
Sample temperature: (25±1)℃
Date of Test: 03/28/2024
Environmental conditions: (24±1) ℃, RH (13±2) %
Mask: An aperture area of 10.011 mm² (M4# Certificate No.: CDjc2023-02145)

The test has been conducted by the PV Metrology Lab of NIM (National Institute of Metrology, China). Measurement of irradiance intensity and all other measurements are traceable to the International System of Units (SI). Data in this report apply only at the time of the test for the sample. For more details, please refer to the text of the report.

	Area (mm^2)	I_{sc}(mA)	V_{oc}(V)	P_{max}(mW)
Reverse Scan	10.011	2.614	1.177	2.554
Forward Scan	10.011	2.614	1.176	2.539
	I_{max}(mA)	V_{max}(V)	FF (%)	η (%)
Reverse Scan	2.504	1.020	83.00	25.51
Forward Scan	2.490	1.020	82.59	25.36

I-V Characterization Methods:
JJF 1622-2017: Calibration Specification of Solar Cells：Photoelectric Properties
Reference Solar Cell:
Type: Mono-Si
Solar Simulator:
Classification: A+AA+ (Double-light source: Xeon and Halogen);
Total irradiance: 1000 W/m² based on I_{sc} of the above Reference Solar Cell.

Report No.: GXgf2024-01375
DUT S/N：122-M4

I-V Characteristic curves and parameters (Reverse & Forward Scan)

Steady-state scanning curve (V_{bias} = 1.020 V, $t_{scaning}$ = 300 s, P_{start}= 2.534 mW and P_{end}= 2.395 mW)

Figure S34. Certification for PSC-PA (Bulk+Surf.). (The certification was carried out by the National Institute of Metrology, China).

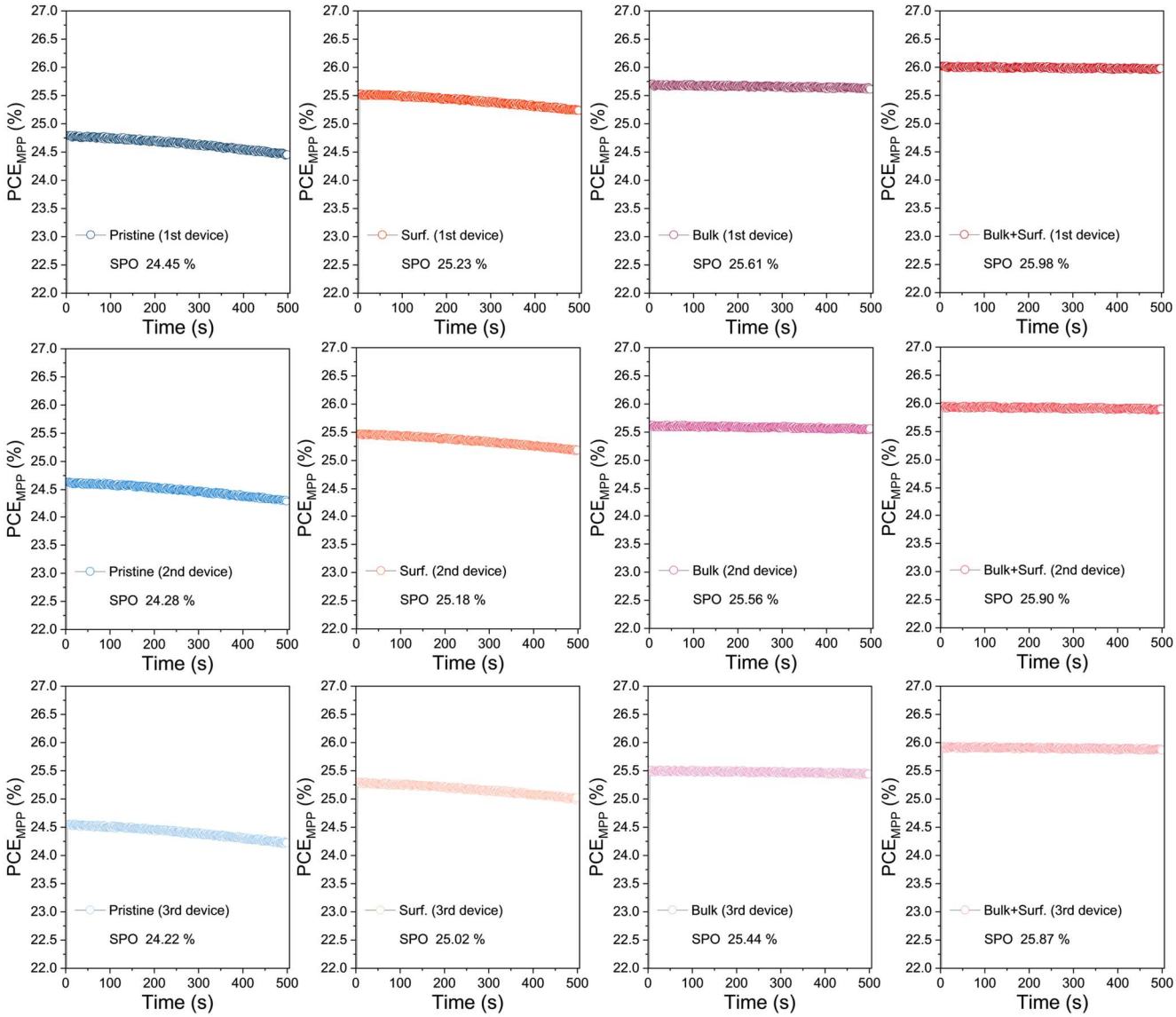

Figure S35. SPO testing (500s) of pristine PSC, PSC-PA (Surf.), PSC-PA (Bulk), and PSC-PA (Bulk+Surf.) devices in air at 25°C. Each type of PSCs includes 3 different devices.

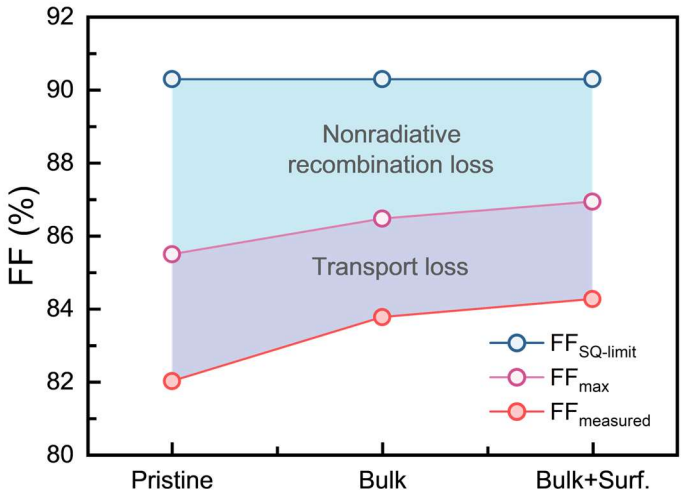

Figure S36. Detailed FF loss analysis of the pristine PSC, PSC-PA (Bulk) and PSC-PA (Bulk+Surf.).

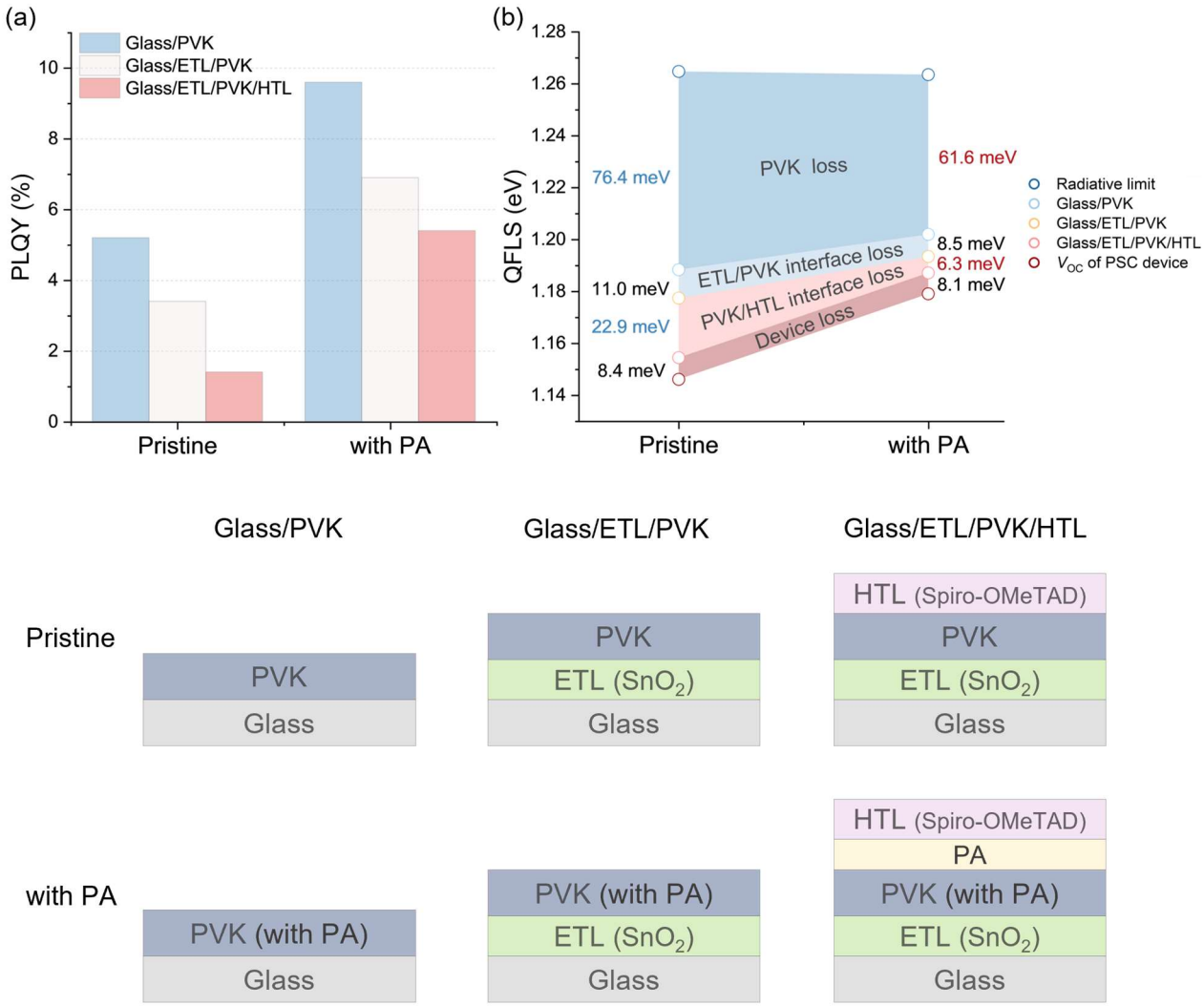

Figure S37 (a) Photoluminescence quantum yield measurements (PLQY) and (b) quasi-Fermi level splitting (QFLS) diagram of pristine PVK and PVK with PA, including the corresponding structure of tested samples.

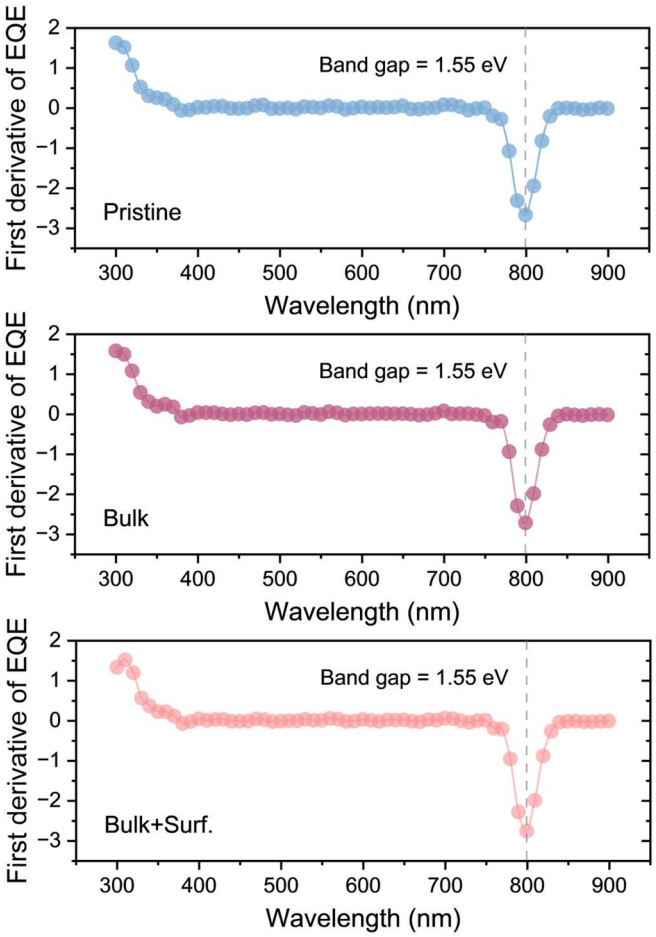

Figure S38 Spectral differential plot of EQE spectrum.

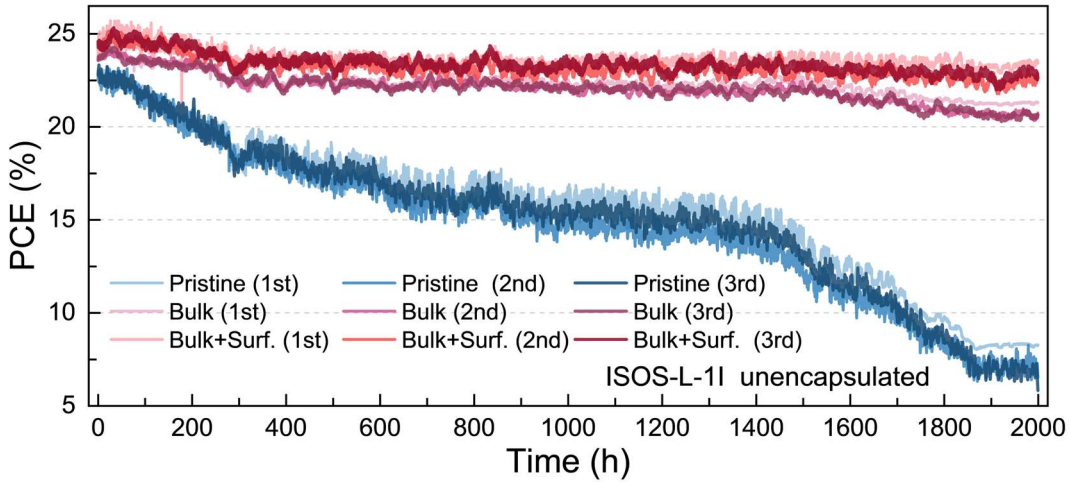

Figure S39. PCE evolution of pristine PSC, PSC-PA (Bulk) and PSC-PA (Bulk+Surf.) using the standard measurement conditions (ISOS-L-1I) under continuous MPP output in N_2 atmosphere for 2000 h. Each type of PSCs includes 3 devices.

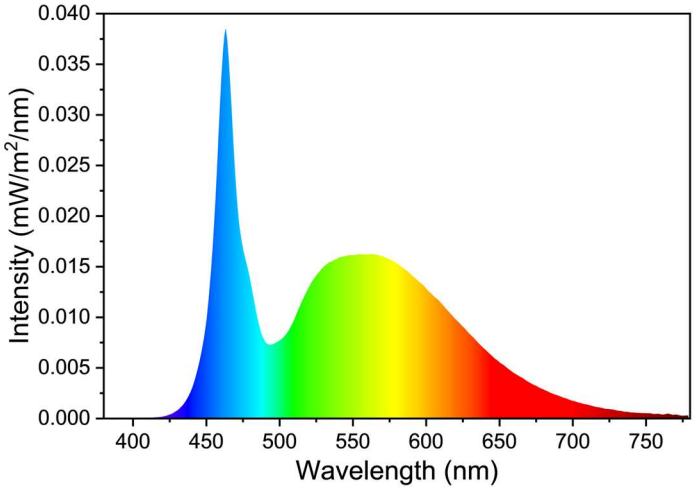

Figure S40. The absolute spectrum of the LED lamp used for MPPT stability testing.

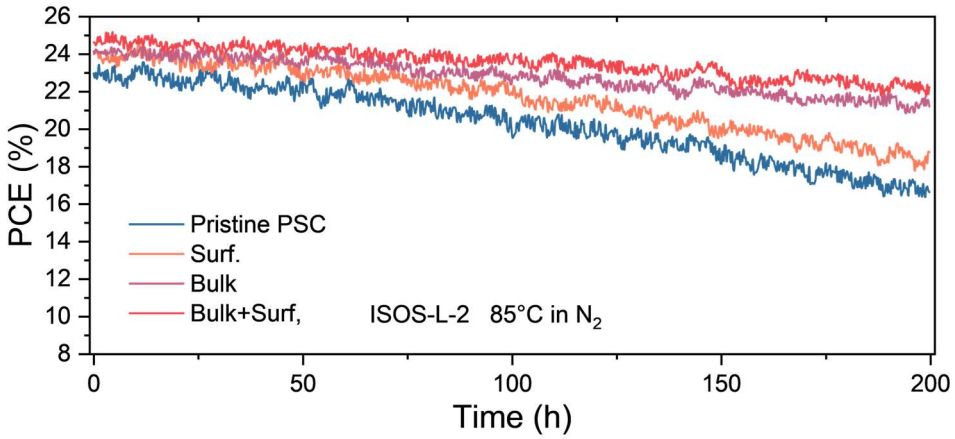

Figure S41. PCE evolution of pristine PSC, PSC-PA (Bulk), PSC-PA (Surf.) and PSC-PA (Bulk+Surf.) using the standard measurement conditions (ISOS-L-2) under continuous MPP output at 85℃ (N_2 atmosphere) for 200 h.

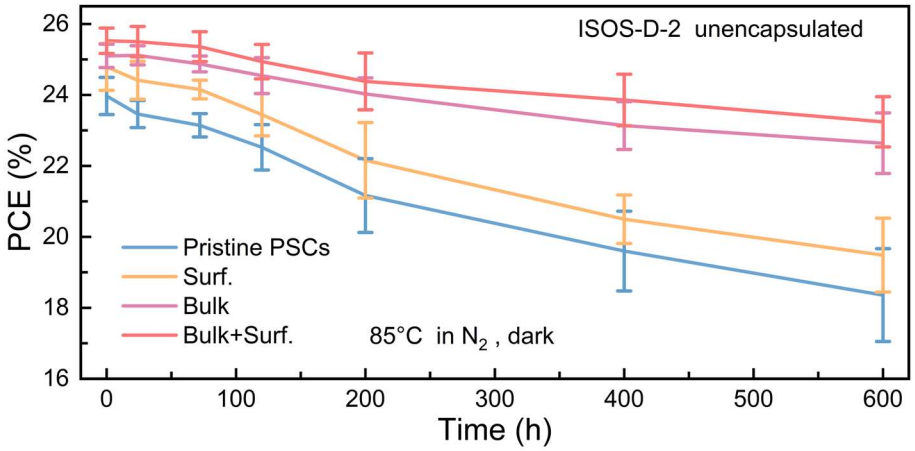

Figure S42. Stability testing of PSCs stored at 85°C (N_2 atmosphere) for 600 h (ISOS-D-2). Each type of PSCs includes 3 devices.

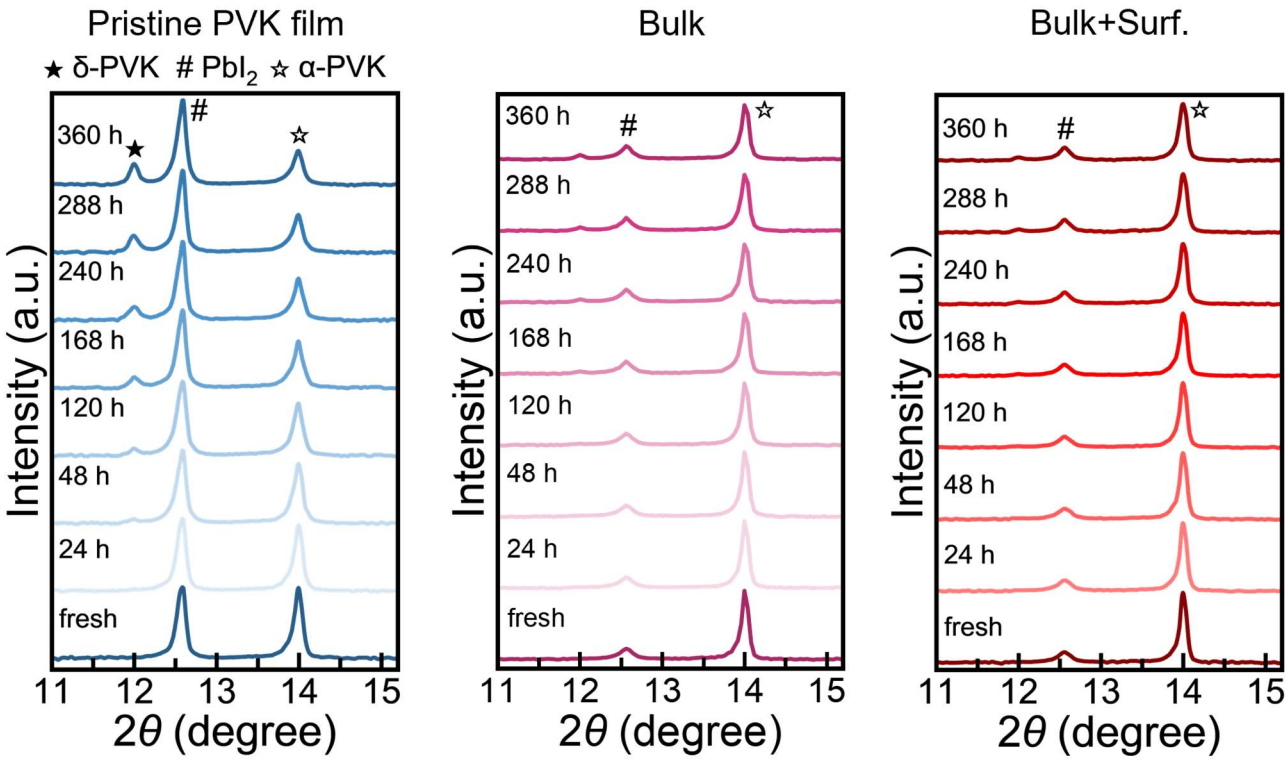

Figure S43. XRD evolution of perovskite films stored in air with 50%-60% RH at 25°C for 360 hours.

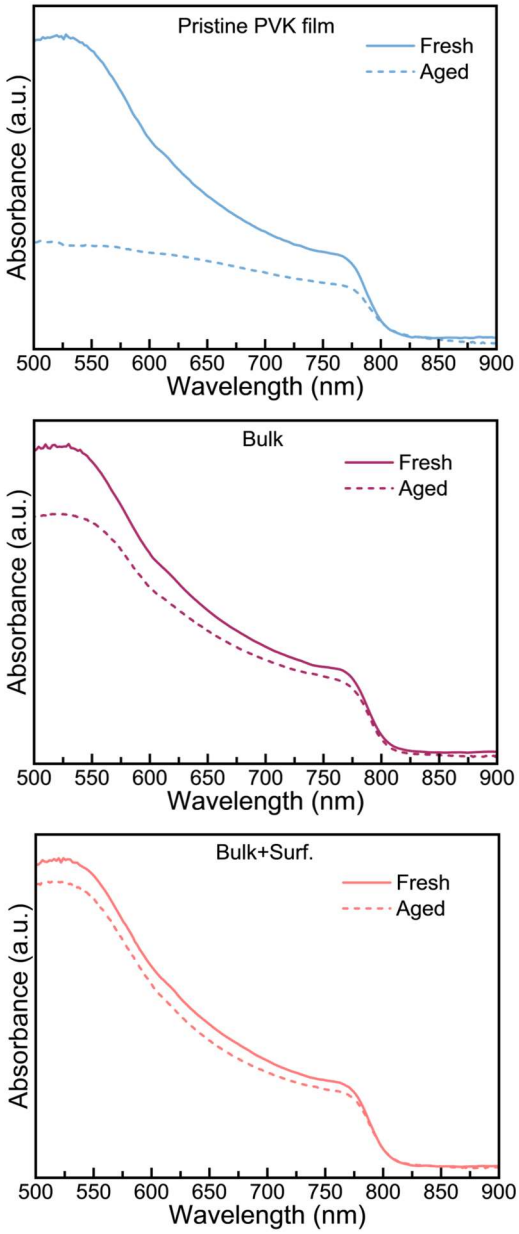

Figure S44. UV-vis spectra of fresh and aged perovskite films stored in air with 70%-80% RH at 25°C for 360 hours.

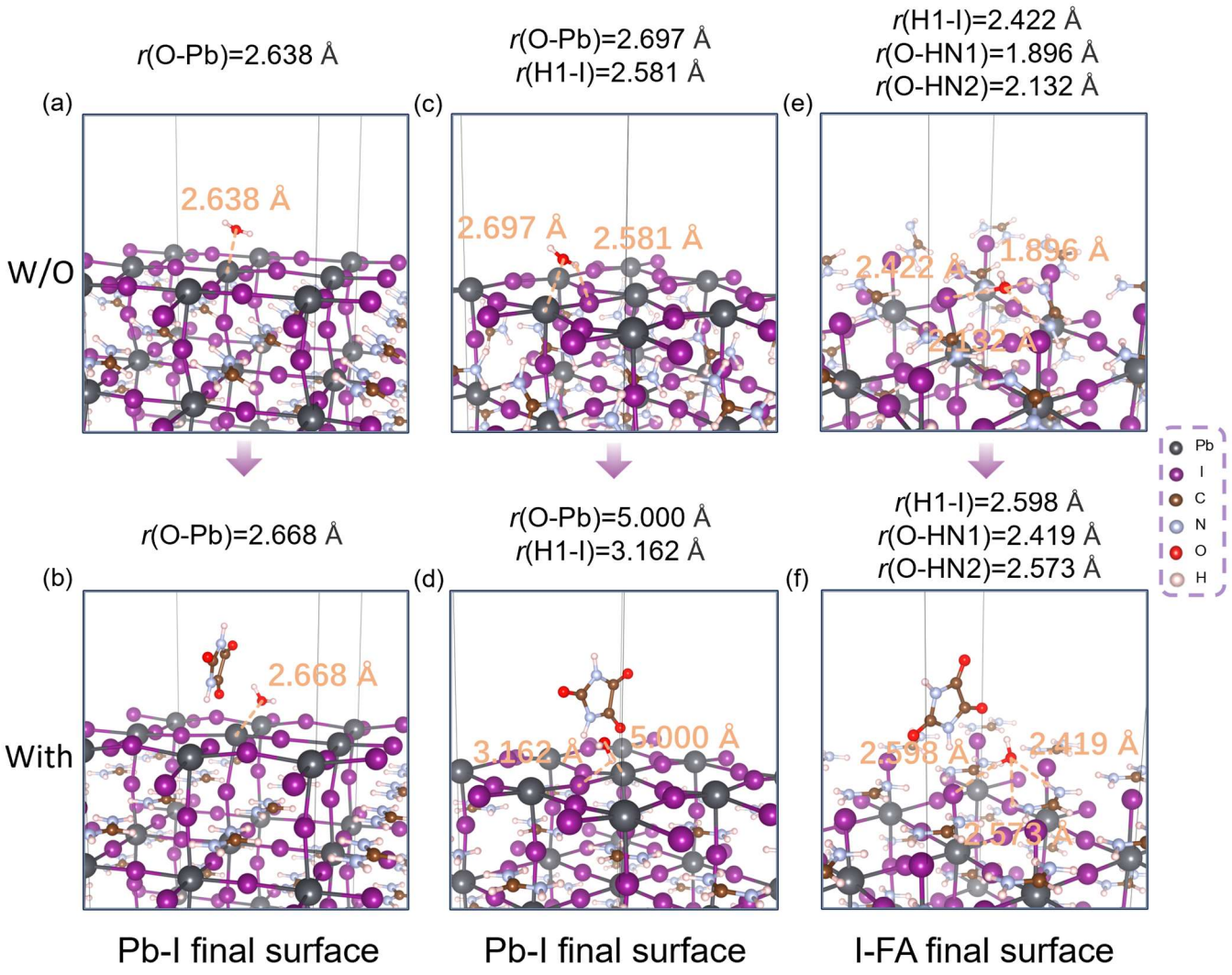

Figure S45. The interaction between H_2O molecules and perovskite obtained from DFT calculation. The theoretical binding models of H_2O to PVK (Pb-I final surface) without and with PA molecule without hydrogen bond involvement are shown in (a) and (b), respectively. The theoretical binding models of H_2O to PVK (Pb-I final surface) without and with PA molecule with hydrogen bond involvement are presented in (c) and (d). The theoretical binding models of H_2O to PVK (I-FA final surface) without and with PA molecule are depicted in (e) and (f).

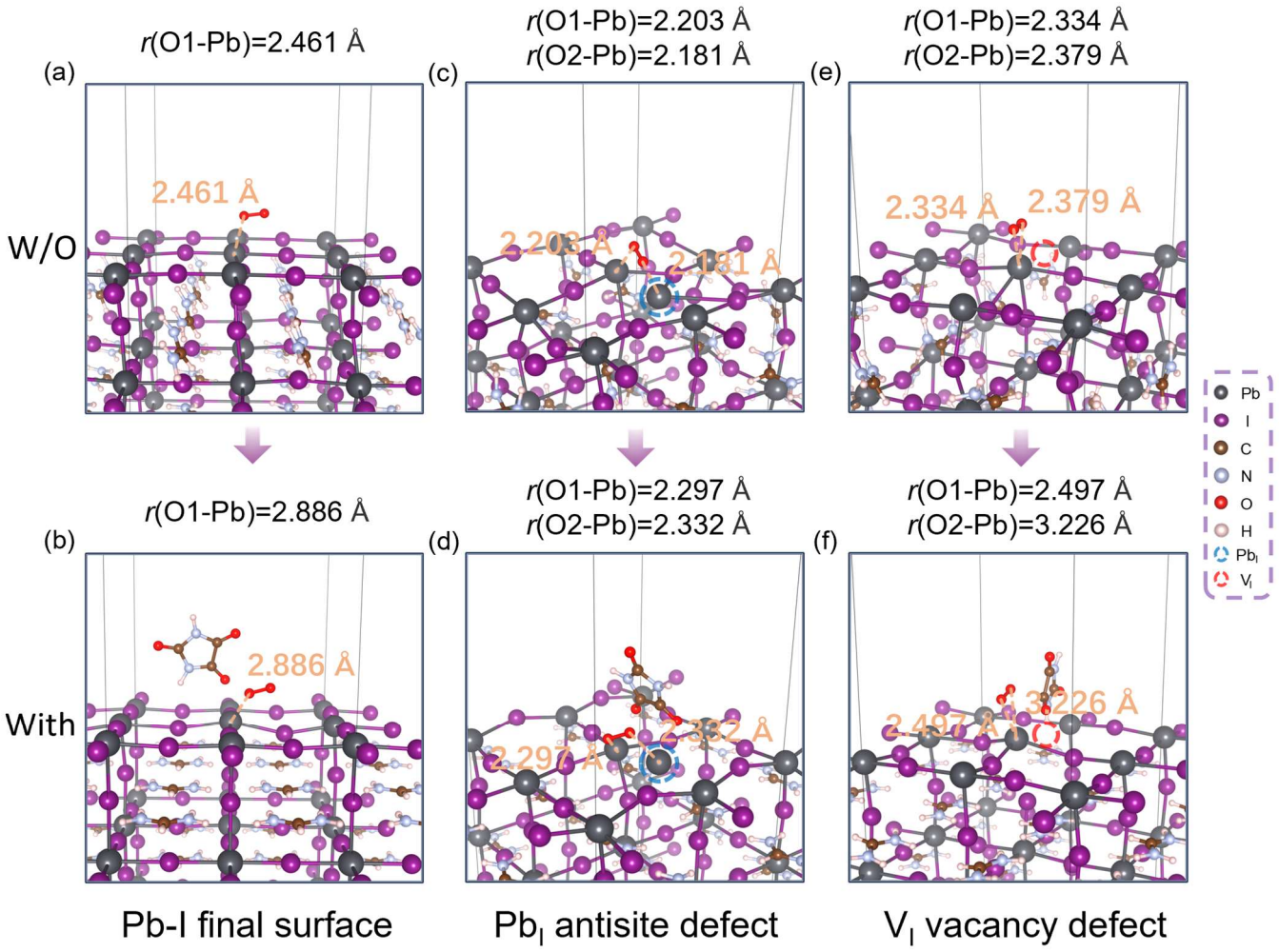

Figure S46. The interaction between O_2 molecules and perovskite obtained from DFT calculation. The theoretical binding models of O_2 to PVK (Pb-I final surface) without and with PA molecule are shown in (a) and (b), respectively. The theoretical binding models of O_2 to PVK (with Pb_I antisite defect) without and with PA molecule are presented in (c) and (d). The theoretical binding models of O_2 to PVK (with V_I vacancy defect) without and with PA molecule are depicted in (e) and (f).

Table S1 Photovoltaic parameters of champion pristine PSC and champion PSC-PA devices under forward voltage scan and reverse voltage scan.

	J_{SC} (mA•cm^{-2})	V_{OC} (V)	*FF* (%)	PCE (%)	HI
Pristine-Forward	26.01	1.125	77.09	22.56	0.083
Pristine-Reverse	26.16	1.146	82.01	24.59	
Bulk-Forward	26.21	1.144	82.94	24.87	0.027
Bulk-Reverse	26.33	1.158	83.77	25.54	
Bulk+Surf.-Forward	26.25	1.173	83.26	25.64	0.015
Bulk+Surf.-Reverse	26.20	1.179	84.27	26.03	

Table S2 The average photovoltaic parameters and their corresponding standard deviations for pristine PSCs and PSCs-PA (Bulk) with varying PA concentrations (15 devices per group).

Devices	Concentration of PA (mg•ml^{-1})	average J_{SC} (mA•cm^{-2})	average V_{OC} (V)	average *FF* (%)	average PCE (%)
Pristine PSCs	0	26.17 (±0.23)	1.131 (±0.008)	80.40 (±1.29)	23.79 (±0.49)
PSCs-Bulk	0.4	26.18 (±0.21)	1.144 (±0.009)	80.64 (±1.19)	24.14 (±0.48)
	0.8	26.18 (±0.21)	1.150 (±0.008)	81.57 (±1.13)	24.56 (±0.43)
	1.2	26.17 (±0.22)	1.156 (±0.008)	82.10 (±0.92)	24.83 (±0.46)
	1.4	26.16 (±0.22)	1.149 (±0.008)	81.75 (±1.15)	24.58 (±0.46)
	3	26.17 (±0.22)	1.144 (±0.011)	80.66 (±1.23)	24.15 (±0.47)

Table S3 The average photovoltaic parameters and their corresponding standard deviations for pristine PSCs and PSCs-PA (Surf.) with varying PA concentrations (15 devices per group).

Devices	Concentration of PA ($mmol•L^{-1}$)	average J_{SC} ($mA•cm^{-2}$)	average V_{OC} (V)	average *FF* (%)	average PCE (%)
Pristine PSCs	0	26.17 (±0.21)	1.131 (±0.009)	80.41 (±1.21)	23.79 (±0.47)
PSCs-Surf.	10	26.17 (±0.21)	1.142 (±0.008)	80.91 (±1.27)	24.18 (±0.49)
	20	26.17 (±0.20)	1.151 (±0.006)	81.54 (±0.98)	24.56 (±0.35)
	30	26.17 (±0.19)	1.158 (±0.007)	82.18 (±0.87)	24.89 (±0.29)
	40	26.17 (±0.19)	1.151 (±0.007)	81.90 (±1.00)	24.66 (±0.46)
	60	26.16 (±0.21)	1.141 (±0.010)	80.79 (±1.38)	24.11 (±0.55)

Table S4 The average photovoltaic parameters and their corresponding standard deviations for pristine PSCs and PSCs-PA (Bulk+Surf.) with varying PA concentrations (15 devices per group).

Devices	Concentration of PA		average J_{SC} ($mA•cm^{-2}$)	average V_{OC} (V)	average *FF* (%)	average PCE (%)
	Bulk ($mg•ml^{-1}$)	Surf. ($mmol•L^{-1}$)				
Pristine PSCs	0	0	26.18 (±0.22)	1.131 (±0.009)	80.40 (±1.37)	23.80 (±0.56)
PSCs-Bulk	1.2	0	26.17 (±0.20)	1.156 (±0.009)	82.11 (±1.07)	24.83 (±0.46)
PSCs-Bulk+Surf.	1.2	10	26.19 (±0.18)	1.159 (±0.008)	82.82 (±0.98)	25.14 (±0.33)
	1.2	20	26.18 (±0.18)	1.165 (±0.005)	83.47 (±0.77)	25.46 (±0.22)
	1.2	30	26.18 (±0.20)	1.169 (±0.006)	83.83 (±0.83)	25.66 (±0.20)
	1.2	40	26.18 (±0.20)	1.165 (±0.006)	83.33 (±0.88)	25.41 (±0.28)
	1.2	60	26.17 (±0.21)	1.151 (±0.01)	82.44 (±1.22)	24.84 (±0.41)

Table S5 The TRPL parameters extracted from Fig. S25b.

Structure	Types of PVK	A_1	τ_1 (ns)		
Glass/PVK	Pristine	1.108	301.3		
	Bulk	1.014	676.9		
	Bulk+Surf.	0.858	1066.9		
	Types of PVK	A_1	τ_1 (ns)	A_2	τ_2 (ns)
Glass/FTO/SnO_2/PVK/Spiro-OMeTAD	Pristine	4.94	33.48	0.53	154.34
	Bulk	3.76	46.12	0.28	259.26
	Bulk+Surf.	12.66	25.65	0.20	335.20

References

1. G. Kresse and J. Furthmuller, *Physical Review B*, 1996, **54**, 11169-11186.
2. G. Kresse and D. Joubert, *Physical Review B*, 1999, **59**, 1758-1775.
3. J. P. Perdew, K. Burke and Y. Wang, *Physical Review B*, 1996, **54**, 16533-16539.
4. S. Grimme, *Journal of Computational Chemistry*, 2006, **27**, 1787-1799.
5. G. Liu, X. Jiang, Y. He, C.-H. Kuan, G. Yang, W. Feng, X. Chen and W.-Q. Wu, *Angewandte Chemie-International Edition*, 2025, **64**, e202419183.
6. G. W. T. M. J. Frisch, H. B. Schlegel, G. E. Scuseria, M. A. Robb, J. R. Cheeseman, G. Scalmani, V. Barone, B. Mennucci, G. A. Petersson, H. Nakatsuji, M. Caricato, X. Li, H. P. Hratchian, A. F. Izmaylov, J. Bloino, G. Zheng, J. L. Sonnenberg, M. Hada, M. Ehara, K. Toyota, R. Fukuda, J. Hasegawa, M. Ishida, T. Nakajima, Y. Honda, O. Kitao, H. Nakai, T. Vreven, J. A. Montgomery, Jr., J. E. Peralta, F. Ogliaro, M. Bearpark, J. J. Heyd, E. Brothers, K. N. Kudin, V. N. Staroverov, R. Kobayashi, J. Normand, K. Raghavachari, A. Rendell, J. C. Burant, S. S. Iyengar, J. Tomasi, M. Cossi, N. Rega, J. M. Millam, M. Klene, J. E. Knox, J. B. Cross, V. Bakken, C. Adamo, J. Jaramillo, R. Gomperts, R. E. Stratmann, O. Yazyev, A. J. Austin, R. Cammi, C. Pomelli, J. W. Ochterski, R. L. Martin, K. Morokuma, V. G. Zakrzewski, G. A. Voth, P. Salvador, J. J. Dannenberg, S. Dapprich, A. D. Daniels, Ö. Farkas, J. B. Foresman, J. V. Ortiz, J. Cioslowski, and D. J. Fox, *Journal*, 2009.
7. S. Pongampai, P. Pakawanit, T. Charoonsuk and N. Vittayakorn, *Nano Energy*, 2021, **90**, 106629.
8. W. Hui, L. Chao, H. Lu, F. Xia, Q. Wei, Z. Su, T. Niu, L. Tao, B. Du, D. Li, Y. Wang, H. Dong, S. Zuo, B. Li, W. Shi, X. Ran, P. Li, H. Zhang, Z. Wu, C. Ran, L. Song, G. Xing, X. Gao, J. Zhang, Y. Xia, Y. Chen and W. Huang, *Science*, 2021, **371**, 1359-1364.
9. W. Abu Laban and L. Etgar, *Energy & Environmental Science*, 2013, **6**, 3249-3253.
10. J. Liang, X. Hu, C. Wang, C. Liang, C. Chen, M. Xiao, J. Li, C. Tao, G. Xing, R. Yu, W. Ke and G. Fang, *Joule*, 2022, **6**, 816-833.
11. Q. Cao, Y. Li, H. Zhang, J. Yang, J. Han, T. Xu, S. Wang, Z. Wang, B. Gao, J. Zhao, X. Li, X. Ma, S. M. Zakeeruddin,

W. E. I. Sha, X. Li and M. Graetzel, *Science Advances*, 2021, **7**, eabg0633.

12. B. Yang, J. Suo, F. Di Giacomo, S. Olthof, D. Bogachuk, Y. Kim, X. Sun, L. Wagner, F. Fu, S. M. Zakeeruddin, A. Hinsch, M. Gratzel, A. Di Carlo and A. Hagfeldt, *Acs Energy Letters*, 2021, **6**, 3916-3923.
13. J. Wu, R. Zhu, G. Li, Z. Zhang, J. Pascual, H. Wu, M. H. Aldamasy, L. Wang, Z. Su, S.-H. Turren-Cruz, R. Roy, F. A. Alharthi, A. Alsalme, J. Zhang, X. Gao, M. Saliba, A. Abate and M. Li, *Advanced Materials*, 2024, **36**, 2407433.
14. M. A. Green, *Solar Cells*, 1982, **7**, 337-340.
15. C. Ma and N.-G. Park, *Chem*, 2020, **6**, 1254-1264.
16. S. Zhang, S. M. Hosseini, R. Gunder, A. Petsiuk, P. Caprioglio, C. M. Wolff, S. Shoaee, P. Meredith, S. Schorr, T. Unold, P. L. Burn, D. Neher and M. Stolterfoht, *Advanced Materials*, 2019, **31**, 1901090.
17. Z. Liu, R. Lin, M. Wei, M. Yin, P. Wu, M. Li, L. Li, Y. Wang, G. Chen, V. Carnevali, L. Agosta, V. Slama, N. Lempesis, Z. Wang, M. Wang, Y. Deng, H. Luo, H. Gao, U. Rothlisberger, S. M. Zakeeruddin, X. Luo, Y. Liu, M. Graetzel and H. Tan, *Nature Materials*, 2025, **24**, 252–259.
18. L. Krueckemeier, U. Rau, M. Stolterfoht and T. Kirchartz, *Advanced Energy Materials*, 2020, **10**, 1902573.
19. U. Rau, *Physical Review B*, 2007, **76**, 085303.
20. M. V. Khenkin, E. A. Katz, A. Abate, G. Bardizza, J. J. Berry, C. Brabec, F. Brunetti, V. Bulovic, Q. Burlingame, A. Di Carlo, R. Cheacharoen, Y.-B. Cheng, A. Colsmann, S. Cros, K. Domanski, M. Dusza, C. J. Fell, S. R. Forrest, Y. Galagan, D. Di Girolamo, M. Graetzel, A. Hagfeldt, E. von Hauff, H. Hoppe, J. Kettle, H. Koebler, M. S. Leite, S. Liu, Y.-L. Loo, J. M. Luther, C.-Q. Ma, M. Madsen, M. Manceau, M. Matheron, M. McGehee, R. Meitzner, M. K. Nazeeruddin, A. F. Nogueira, C. Odabasi, A. Osherov, N.-G. Park, M. O. Reese, F. De Rossi, M. Saliba, U. S. Schubert, H. J. Snaith, S. D. Stranks, W. Tress, P. A. Troshin, V. Turkovic, S. Veenstra, I. Visoly-Fisher, A. Walsh, T. Watson, H. Xie, R. Yildirim, S. M. Zakeeruddin, K. Zhu and M. Lira-Cantu, *Nature Energy*, 2020, **5**, 35-49.